RESEARCH ACTIVITIES

Materials Molecular Science

Extensive development of new molecules, molecular systems and their higher-order assemblies is being conducted in the four divisions and in the research center for molecular scale nanoscience. Their electronic, optical and magnetic properties as well as reactivities and catalytic activities are being examined in an attempt to discover new phenomena and useful functions.

Structures and Functions of Metal–Carbon Nano-Systems Produced from Metal-Acetylides

Department of Materials Molecular Science
Division of Electronic Structure

NISHI, Nobuyuki	Professor
JUDAI, Ken	Assistant Professor
NISHIJO, Junichi	Assistant Professor
OISHI, Osamu	Technical Associate
FURUYA, Ari	Post-Doctoral Fellow
NUMAO, Shigenori	Graduate Student
UBAHARA, Wakana	Secretary

Metal acetylides or metal ethynyl conpounds are made of the M^+–C^- ionic bonds. However, the ionic states of the acetylides are essentially metastable resulting in the segregation into metal-carbon or metal-organic polymer nanophases. This segregation still maintains M^+–C^- ionic bonds around the interfaces of the metal wire, particles, and dendroid sponges exhibiting various functions depending on the metal species. Removal of the metals produces two types of carbon materials: One is mesoporous carbon with graphene walls and the other is amorphous carbon containing small amount of metals.

1. A Novel Functional Carbon Material: Mesoporous Carbon Nano-Dendrite with Graphene Walls

We have succeeded to synthesize a new material, Mesoporous Carbon Nano-Dendrites (MCNDs) with graphenen walls. The novel material exhibits good electric conductance due to large particle sizes and excellent ion fluidity. These properties could be attributed to the dendriform branching structure of the main bodies. Silver acetylide (Ag_2C_2) produces dendriform nanostructures under ultrasonic irradiation. The dendrites were quickly warmed to 150 °C emitting a brilliant flash of reddish orange lighting and thunderous sound indicative of the sudden jump of the local temperature to higher than 2000 °C. This sudden heating boils off the silver from the main body, leaving MCNDs. Raman spectra clearly indicate that the bodies consist of mainly single-layer graphene walls. Scanning Electron Microscope (SEM) and Transmission Electron Microscope (TEM) images as well as EELS spectra show that the main bodies with ~50 nm radii ramifies at every 100–150 nm and composed of the cells with graphene walls. Figure 1a shows a SEM image of MCND. The MCNDs showed a BET surface area of 1600~1800 m^2/g. As shown in Figure 1b, cyclic voltammetry of the supercapacitor with MCND electrodes exhibited good rectangular curves, even at a scanning rate of 400 mV/s, suggesting applicability for high current and high-speed charge-discharge capacitors for motor vehicles. By filling metallic layers or cluster islands in the pores, one can utilize the extremely large surface area for the electrodes of lithium ion batteries or fuel cells, respectively.

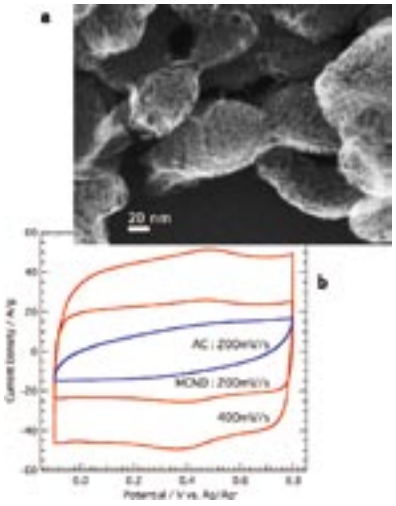

Figure 1. **a**: a high resolution SEM image of the edge region of MCND. **b**: Cyclic voltammograms of a MCND EDLC with an electrode thickness of 80 μm. Although the commercial activated carbon never shows a rectangular response with changing potentials at a scan rate faster than 50 mV/s, MCND can afford high-speed charge-discharge performance at a rate faster than 400 mV/s and current densities higher than 40 A/g.

2. Amorphous Carbon Material Converted from Self-Assembled Copper Acetylide Nanowires

In the next case, we deal with copper acetylide (Cu_2C_2) nanowires as less explosive nano-materials. Cu_2C_2 has been well-known as explosive substance. However, decreasing the size of material into the nanometer makes it possible to control

the explosive segregation reaction. We suggest a new method to produce amorphous carbon material by lower temperature process converted from the less explosive Cu_2C_2 nanowires. Amorphous carbon is normally produced with high temperature process of carbonization. An explosive nature of Cu_2C_2 itself provides segregation reaction into elemental carbon and copper at a temperature below 150 °C. The product by this low temperature process shows unique spectroscopic characters and material properties.

It is very simple to produce Cu_2C_2 nanowires. The fabrication method for Cu_2C_2 nanowire involves bubbling acetylene (C_2H_2) gas into an ammonia solution of copper chloride (CuCl). When the C_2H_2 reacts slowly, Cu_2C_2 molecules can self-assemble into nanowires 5 nm in diameter. Gradual heating of the product up to 150 °C for 1–5 hours in a vacuum transforms Cu_2C_2 nanowire into elemental copper and carbon via a segregation reaction without explosion. Aqueous NH_3 or nitric acid treatment can separate amorphous carbon from Cu element dissolving in solution.

Figure 2 shows Raman spectra of various carbon materials. Graphite displayed sharp peak around 1575 cm^{-1}, which could be assigned to G band of inherent in graphite lattices. For more poorly crystallized graphite, an additional broad band appears at 1350 cm^{-1} (so-called D band. Raman spectra demonstrated difference of crystalline characters between graphite and activated carbon. The amorphous carbon converted from Cu_2C_2 nanowires exhibits no distinct peak in the Raman spectrum. The spectroscopic study tells us that the low temperature process can generate genuine amorphous carbon materials without any trace of crystalline graphite. We attempt this new amorphous carbon evaluated to the application as hydrogen storage and so on right now.

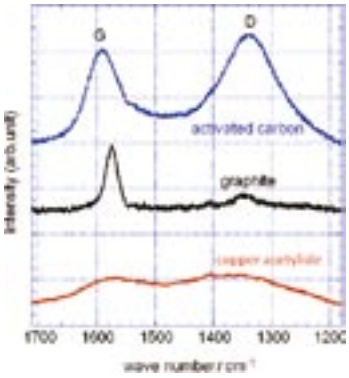

Figure 2. Raman spectra of various carbon materials. Graphite (black line, middle) shows a sharp G band at 1575 cm^{-1}, and active carbon (blue line, top) gives broad G band and also broad D band around 1350 cm^{-1}. Amorphous carbon converted from Cu_2C_2 nanowires shows extremely broad band (red line, bottom).

3. Surface Environment of Ag Nanoparticles Formed by Decomposition of Silver Phenylacetylide

Recently, we developed a facile preparation method of one dimensional Ag nanoparticle arrays via thermal- or photo-decomposition of silver phenylacetylide (Ag–C≡C–Ph). The nanoparticle is stabilized by the surface organic layer which keeps the nanoparticles from aggregation and oxidation. The structure of the surface layer was investigated by surface enhanced Raman spectroscopy and IR spectroscopy.

Figure 3 shows the Raman spectra of as-prepared, thermal- and photo-decomposed Ag–C≡C–Ph. Decomposed samples clearly show broad peaks at around 1970 cm^{-1} regardless of the decomposition process. The peaks are characteristic of the C≡C stretching mode of a surface adsorbed phenylacetylide anion, and indicates that the surface of the Ag nanoparticle is covered with vertically adsorbed phenylacetylene molecules. The peak shows no significant change even after 12 h thermal- or photo- decomposition, indicating the quite strong interaction between Ag nanoparticles and surface adsorbed molecules. Phenylacetylenes except surface adsorbed molecules are rapidly dimerized in decomposition processes to 1,4-diphenylbutadiyne which shows Raman and IR peaks of in- and out-phase =C≡C–C≡C= stretching at 2215 and 2150 cm^{-1}, respectively. In the case of long-time UV irradiated sample, the polymerization continues and results in the graphitic structure as evidenced by the occurrence of D- and G-bands in Raman spectrum at around 1350 and 1580 cm^{-1}, respectively, while the peak of –C≡C–C≡C– in-phase stretching disappears. In contrast, polymerization of 1,4-diphenylbutadiyne is rare in the case of after 12 h heat treatment at 150 °C, where only a small amount of graphitic structure is observed as shown in Figure 3. These results suggest that we can control not only the nanoparticle size of one dimensional Ag arrays but also the conductivity of its intermediate organic matrix from insulating to metallic, in which the Ag nanoparticles are firmly protected by surface adsorbed phenylacetylenes from chemical reactions.

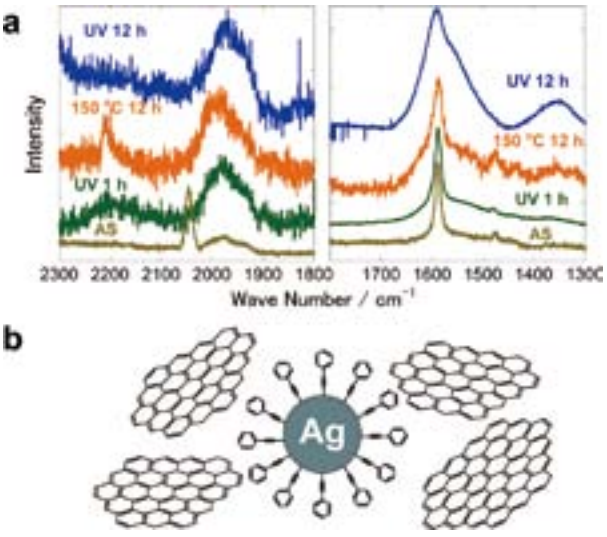

Figure 3. a) Raman spectra of as-prepared and decomposed Ag–C≡C–Ph. b) Schematic drawing of decomposed Ag–C≡C–Ph after 12 h UV irradiation.

Awards

JUDAI, Ken; Young Best presenter Award, 6th Annual Meeting of Society of Nano Science and Technology.
NUMAO, Shigenori; Young Best presenter Award, 6th Annual Meeting of Society of Nano Science and Technology.

Characterization of Magnetic Ultrathin Films by Novel Spectroscopic Methods

Department of Materials Molecular Science
Division of Electronic Structure

YOKOYAMA, Toshihiko	Professor
NAKAGAWA, Takeshi	Assistant Professor
TAKAGI, Yasumasa	Assistant Professor
YAMAMOTO, Isamu	Post-Doctoral Fellow
ISAMI, Kyohei	Graduate Student
NOTO, Madomi	Secretary

Novel properties of magnetic metal ultrathin films have been attractive both from fundamental interest and from technological requirements. We are interested in drastic modification of metal thin films by surface chemical treatment such as adsorption-induced spin transitions and morphological changes. The magnetic properties are characterized by means of several kinds of spectroscopic methods like MOKE (Magneto-Optical Kerr Effect) using lasers and XMCD (X-ray Magnetic Circular Dichroism) using synchrotron radiation. In 2007, we have installed an *in situ* XMCD system with a superconducting magnet (up to 7 T) and a liq. He cryostat (down to 5 K). Some results obtained by the XMCD system are described below.

We are also exploiting new techniques of ultrafast time resolved ultraviolet (UV) magnetic circular dichroism (MCD) photoelectron emission microscopy (PEEM) in order to perform spatiotemporal magnetic imaging. Moreover, we are developing a two-photon photoemission MCD technique including PEEM.

1. First Observation of Ultrafast UV Magnetic Circular Dichroism Photoemission Electron Microscope Images

In 2006, we discovered surprising enhancement of the visible/ultraviolet photoemission MCD from ultrathin Ni films on Cu(001) when the photon energy was tuned to the work function threshold.[1)] Based on this discovery, we succeeded in the first observation of UV MCD PEEM images of ultrathin magnetic films.[2)] This method allows us to do in-laboratory MCD PEEM measurements instead of the usage of synchrotron radiation XMCD PEEM. Moreover, when ultrashort pulsed lasers are employed, pump-and-probe UV MCD PEEM measurements provide us a time resolving power of ~100 fs rather easily, which is two to three orders of magnitude faster than that of XMCD PEEM.

Since 2007 we have been reconstructing the measurement system by installing an ultrashort-pulsed deep UV laser and new UHV chambers to combine the MOKE, PEEM and photoemission experiments. Although the system is still under construction, we have tentatively observed time-resolved UV MCD PEEM images by using the previous setup. This work is a collaboration with Profs. Kazuya Watanabe and Yoshiyasu Matsumoto in Kyoto University.

Ultrafast UV MCD PEEM images were recorded by means of the pump-and-probe technique, in which the pump and probe lights were respectively the linearly-polarized fundamental (800 nm, ~70 fs) and the circularly-polarized second-order (400 nm, ~200 fs) harmonics of a Ti:sapphire laser. The sample is Cs-coated Ni (12 monolayer) grown epitaxially on Cu(001).

Figure 1 shows the femtosecond time resolved UV MCD PEEM image and the time evolution of the local magnetization observed for the first time. Although the present result is rather tentative, we will measure more beautiful images in near future by using the new apparatus.

Moreover, we have succeeded in the first observation of the two-photon MCD PEEM. By employing a newly installed tunable deep UV laser, the maximum MCD asymmetry was found to be quite large. Especially, at 45° incidence the MCD is maximized, and this is quite useful for two-photon UV MCD PEEM.

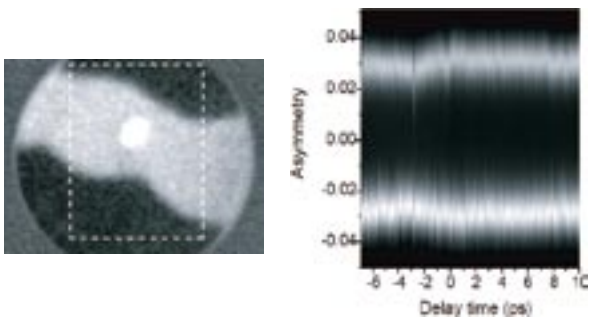

Figure 1. Time resolved UV MCD PEEM image (left, 10μm area) and the time dependence of the local magnetization (right) of Cs-coated Ni(12ML)/Cu(001). Time resolution is ~200 f.

2. X-Ray Magnetic Circular Dichroism under High Magnetic Field and Extremely Low Temperature[3)]

XMCD is a powerful tool for the investigation of magnetism since it provides valuable information on element specific orbital and spin magnetic moments. A XMCD measurement system with a superconducting magnet and a liq. He cryostat is, however, not so popular in the world especially for public usage, although XMCD measurements under high magnetic fields are crucial for the investigation of magnetic anisotropy, because the saturated magnetization along the hard axis can be achieved around several tesla. We have thus constructed an in situ UHV soft X-ray XMCD system.

Figure 2 shows the schematic view and the photo of the present UHV XMCD system, which is usually installed at Beamline 4B of UVSOR-II. The magnetic field applied is ±7 T (typically ±5 T) and the sample temperature is ~5 K using liq. He. Samples are prepared in the preparation chamber and are transferred to the measurement chamber under UHV condition. The polar angle of the sample can be rotated by 360°, allowing us to examine angle dependence of XMCD.

In order to demonstrate the usefulness of the system, we have investigated angle dependent Co *L*-edge XMCD of Co(0.4 ML) on Cu(001). Since the sample shows strong in-plane magnetic anisotropy, the saturation along the perpendicular magnetization direction (hard axis) requires a magnetic field of >3.4 T (5 T was applied). Through the analysis of the angle-dependent XMCD spectra, which can be done with saturated magnetization data even for the hard axis. As a result, the enhancements of the magnetic moments compared to the corresponding bulk values were clearly elucidated: ~15% for the spin magnetic moment, and ~96% and ~53% for the orbital magnetic moments along the surface parallel and normal directions, respectively. The surface magnetization is found to be essentially different from the bulk one.

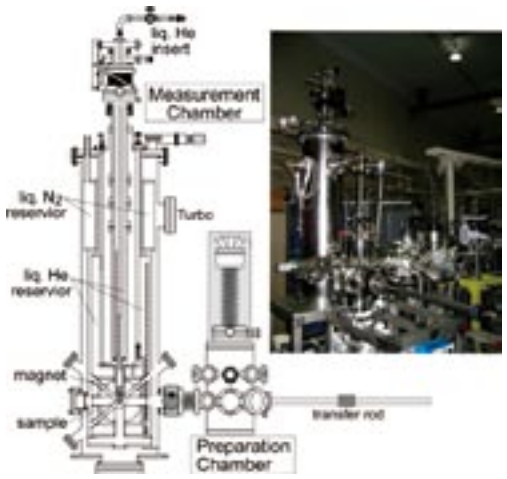

Figure 2. Schematic view and photo of the XMCD system with a superconducting magnet and a liq. He cryostat.

3. Magnetism of Self-Assembled Co Nanorods Grown on Cu(110)-(2x3)N[4)]

Magnetic properties of low dimensional magnets has recently attracted much interest due to their importance for further dense magnetic recording media. In this work, we have investigated magnetic properties of self-assembled Co nanorods grown on Cu(110)-(2×3)N[5)] using the superconducting magnet XMCD system described above. This work was performed in collaboration with Prof. F. M. Leibsle (University of Missouri, Kansas) and Dr. X. -D. Ma and Prof. M. Przybylski (Max-Planck Institut, Halle).

Magnetic properties have been characterized by MOKE and XMCD. Figure 3(a) shows the angular dependence of Co *L*-edge *in situ* XMCD obtained by using the superconducting magnet at 4.9 K. Angle dependent magnetization curves of the Co nanorods recorded by MOKE (not shown) and XMCD [Figure 3(b)] show that the magnetic easy axis is perpendicular to the rod within the substrate plane, irrespective of the Co thickness down to 0.8 ML. From Figure 3(b), one can recognize that a high magnetic field is necessary to magnetize the sample along the magnetic field direction. The analysis of the magnetization curves clarify that the magnetic anisotropy is not dominated by the shape anisotropy but by the magnetocrystalline anisotropy. The XMCD analysis reveals significant enhancement of the orbital magnetic moment along the easy axis compared to the hard axes ([001] > [1$\bar{1}$0] > [110]). The magnetocrystalline anisotropy is found to be directly related to the anisotropy of the orbital magnetic moment.

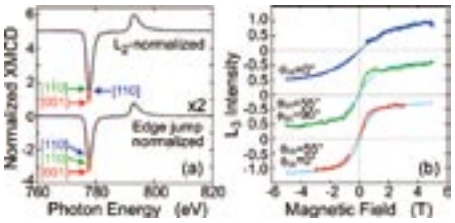

Figure 3. (a) Angle dependent Co *L*-edge XMCD spectra of Co/Cu(110)-(2×3)N (Co 0.8 ML) at T = 4.9 K and H = ±5.0 or ±3.0 T. The lower and upper spectra correspond to those normalized with the edge jumps (×2 magnified) and the L_2 peak top intensity (+5 shifted), respectively. (b) Magnetization curves at T = 4.9 K recorded with the L_3 peak top. The simulated magnetization curves (light blue dotted lines) using a simple magnetic anisotropy model are also shown.

References

1) T. Nakagawa and T. Yokoyama, *Phys. Rev. Lett.* **96**, 237402 (2006).
2) T. Nakagawa, T. Yokoyama, M. Hosaka and M. Katoh, *Rev. Sci. Instrum.* **78**, 023907 (2007).
3) T. Nakagawa, Y. Takagi, Y. Matsumoto and T. Yokoyama, *Jpn. J. Appl. Phys.* **47**, 2132 (2008).
4) X. -D. Ma, T. Nakagawa, Y. Takagi, M. Przybylski, F. M. Leibsle and T. Yokoyama, to be published.
5) S. M. York and F. M. Leibsle, *Phys. Rev. B* **64**, 033411 (2001).

Award

TAKAGI, Yasumasa; Young Researcher Promotion (Wakate-Shourei) Award, The Physical Society of Japan (2007).

Structure and Properties of Metal Clusters Protected by Organic Molecules

Department of Materials Molecular Science
Division of Electronic Structure

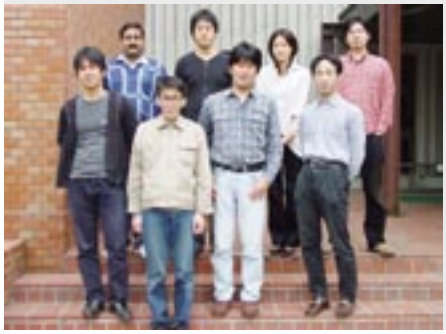

TSUKUDA, Tatsuya	Associate Professor*
NEGISHI, Yuichi	Assistant Professor†
CHAKI, Nirmalya K.	IMS Fellow‡
TSUNOYAMA, Hironori	Post-Doctoral Fellow§
SHICHIBU, Yukatsu	Post-Doctoral Fellow‖
NAKAO, Satoru	Post-Doctoral Fellow
UBAHARA, Wakana	Secretary

1. Origin of Magic Stability of Thiolated Gold Clusters: A Case Study on $Au_{25}(SC_6H_{13})_{18}$[1)]

The present work aims to test the validity of the electronic shell model for $Au_{25}(SC_6H_{13})_{18}$ by monitoring the charge state of the Au:S core and thereby to elucidate the origin of magic stability. Electrospray ionization mass spectrometry revealed that the Schiffrin method yields $[Au_{25}(SC_6H_{13})_{18}]^x$ with a distribution of charge states, which shifts toward negative values with reduction time. The stable ions $[Au_{25}(SC_6H_{13})_{18}]^{1+}$ and $[Au_{25}(SC_6H_{13})_{18}]^{1-}$ can be synthesized by chemical oxidation and reduction of $[Au_{25}(SC_6H_{13})_{18}]^0$, respectively. These findings lead us to conclude that electronic shell closing is not a crucial factor for the high stability of $[Au_{25}(SC_6H_{13})_{18}]^x$ (x = 1–, 0, 1+). We ascribe magic stability to the core-in-cage structure predicted theoretically.

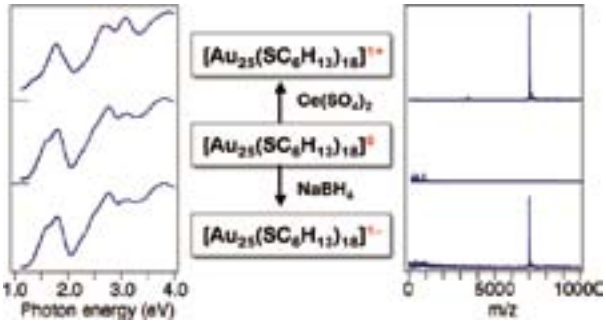

Figure 1. Optical absorption spectra (left) and ESI mass spectra (right) of $[Au_{25}(SC_6H_{18})_{18}]^z$ with different charge states.

2. Ubiquitous 8 and 29 kDa Gold: Alkanethiolate Cluster Compounds: Mass-Spectrometric Determination of Molecular Formulas and Structural Implications[2)]

The molecular formula and charge state distributions of thus-far known, ubiquitous alkanethiolate-protected gold clusters with core-masses of 8 and 29 kDa were assessed using electrospray ionization mass spectrometry (ESI-MS). The 8 and 29 kDa clusters were determined to be composed of single species, $[Au_{38}(SC_n)_{24}]^z$ and $[Au_{144}(SC_n)_{59}]^z$, respectively, with charge states of $z \geq 0$. Possible geometric structures for $Au_{38}(SC_n)_{24}$ and $Au_{144}(SC_n)_{59}$ are discussed based on the structures of relevant systems that have been recently determined experimentally and theoretically; $[Au_{25}(SR)_{18}]^{-1}$ and $Au_{102}(SR)_{44}$, in which the Au cores are protected by monomers [–SR–Au–SR–] and/or dimers [–SR–Au–SR–Au–SR–]. Their preferential formation and chemical robustness are proposed as being associated with high stability due to geometric factors, while the Au-thiolate interface takes on common motifs regardless of the underlying Au core.

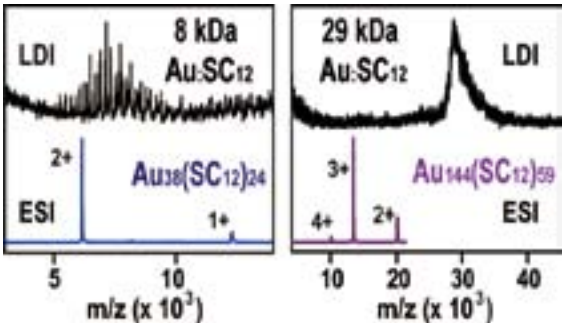

Figure 2. LDI and ESI mass spectra of $[Au_{38}(SC_6H_{18})_{24}]^z$ (left) and $[Au_{144}(SC_6H_{18})_{59}]^z$ (right).

3. Thermosensitive Gold Nanoclusters Stabilized by Well-Defined Vinyl Ester Star Polymers: Reusable and Durable Catalysts for Aerobic Alcohol Oxidation[3)]

Au nanoclusters of less than 4 nm with a narrow size distribution were prepared and supported in thermosensitive vinyl ether star polymers obtained by living cationic polymerization. The thermosensitivity of the star polymers

permitted easy separation of the clusters from the reaction mixture without any negative aggregation. Thus, the Au clusters could be recovered for reuse several times to induce alcohol oxidation with similar reactivity in each run.

4. Ligand exchange of $Au_{25}SG_{18}$ Leading to Functionalized Gold Clusters: Spectroscopy, Kinetics, and Luminescence[4)]

Ligand exchange offers an effective way to modify the properties of the recently prepared quantum clusters of gold. To tune optical and photoluminescence properties of one of the most stable quantum clusters of gold, $Au_{25}SG_{18}$ (SG-glutathione thiolate), we functionalized it by the exchange of -SG with functionalized-SG and with an altogether different ligand, namely, 3-mercapto-2-butanol (MB). The products were characterized by various techniques such as optical absorption (UV-vis), Fourier-transform infrared (FTIR), nuclear magnetic resonance (NMR), X-ray photoelectron (XPS), and luminescence spectroscopies, mass spectrometry, and thermogravimetry (TG). Analyses of the TG data helped to establish the molecular composition of the products. Ligand exchange reaction was monitored by NMR spectroscopy, and it was found that the exchange reaction follows a first order kinetics. The XPS study showed that after the exchange reaction there was no change in the chemical nature of the metal core and binding energy values of Au $4f_{7/2}$ and $4f_{5/2}$, which are similar in both the parent and the exchanged products. Photoluminescence studies of these clusters, done in the aerated conditions, showed that the excitation spectrum of the MB-exchanged product is entirely different from the acetyl- and formyl-glutathione exchanged products. The inherent fluorescence and solid-state emission of these clusters were observed. This intense emission allows optical imaging of the material in the solid state. The emission is strongly temperature dependent. The synthesis of a diverse variety of clusters and their chemical stability and intense luminescence offer numerous applications in areas such as energy transfer, sensors, biolabeling, and drug delivery.

5. Electronic Structure of Dendrimer-Au Hybrid Nanoparticle: Hard X-Ray Photoemission Study[5)]

We have carried out the hard X-ray photoemission study of dendrimer-Au hybrid nanoparticles/nanoclusters supported on the HOPG substrates. From the detailed line-shape analysis for Au 4f core-level photoemission spectrum of dendrimer-Au hybrid nanoparticles with mean diameter of 2.6 nm, it is found that Au 4f core-level spectrum consists of three components. We attribute these components to the interior Au atoms, surface Au atoms, and surface Au atoms bonded to dendrimers. Furthermore, we have investigated the valence-band photoemission spectra. From these results, we discuss the electronic structures and interfacial properties of dendrimer-Au hybrid nanoparticles/nanoclusters.

References

1) Y. Negishi, N. K. Chaki, Y. Shichibu, R. L. Whetten and T. Tsukuda, *J. Am. Chem. Soc.* **129**, 11322–11323 (2007).
2) N. K. Chaki, Y. Negishi, H. Tsunoyama, Y. Shichibu and T. Tsukuda, *J. Am. Chem. Soc.* **130**, 8608–8610 (2008).
3) S. Kanaoka, N. Yagi, Y. Fukuyama, S. Aoshima, H. Tsunoyama, T. Tsukuda and H. Sakurai, *J. Am. Chem. Soc.* **129**, 12060–12061 (2007).
4) E. S. Shibu, M. A. Habeeb Muhammed, T. Tuskuda and T. Pradeep, *J. Phys. Chem. C* **112**, 12168–12176 (2008).
5) Y. Murase, T. Kitagawa, M. Imamura, A. Tanaka, H. Yasuda, Y. Negishi, T. Tsukuda, S. Ueda, Y. Yamashita, H. Yoshikawa and K. Kobayashi, *Trans. Mater. Res. Soc. Jpn.* **33**, 169–172 (2008).

Award

NEGISHI, Yuichi; The Chemical Society of Japan Award for Young Chemists.

* Present Position; Professor, Catalysis Research Center, Hokkaido University, Sapporo 001-0021
† Present Address; Tokyo University of Sciences, Tokyo 162-8601
‡ Present Address; The Pennsylvania State University, Pennsylvania 16802, U. S. A.
§ Present Address; Catalysis Research Center, Hokkaido University, Sapporo 001-0021
|| Present Address; Hokkaido University, Sapporo 068-0810

Optical Studies of Charge Ordering in Organic Conductors

Department of Materials Molecular Science
Division of Electronic Properties

YAKUSHI, Kyuya	Professor
YAMAMOTO, Kaoru	Assistant Professor
URUICHI, Mikio	Technical Associate
KOWALSKA, Aneta	JSPS Post-Doctoral Fellow
NAKANO, Chikako	Research Fellow
YUE, Yue	Graduate Student
ABE, Hitomi	Secretary

In many organic charge-transfer salts, the electronic state of charge carriers is located at the boundary between localized and delocalized states. Recently the charge ordering (CO) originated from the localization due to Coulomb interaction is widely found in organic conductors, and the electronic phase diagrams of typical organic conductors are re-considered taking CO into account. We are interested in the CO state, first because a CO phase is neighbored on a superconducting phase, wherein a charge-mediated superconductivity is theoretically predicted, second because some compounds in a CO phase shows ferroelectricity, the origin of which is attributable to the electron displacement, third because the narrow-band compounds have an inhomogeneous intermediate state between metallic and CO states, which is not well understood. We employ infrared and Raman spectroscopy to study the CO state.

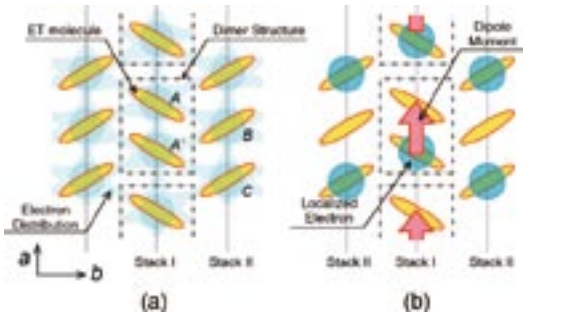

Figure 1. Schematic views of the arrangement of ETs and electrons. (a) In the metallic phase ($T > T_{CO}$), electrons are delocalized, and thus each ET has +0.5e. (b) In the charge ordered insulator phase ($T < T_{CO}$), charges are localized on some ETs. Because of finite alternation in Stack I, dipole moments between *A* and *A*' (solid arrows) survives in the unit cell.

1. Strong Optical Nonlinearity and Its Ultrafast Response Associated with Electron Ferroelectricity in an Organic Conductor[1)]

We yielded an experimental evidence for spontaneous generation of electric polarization in an organic conductor α-$(ET)_2I_3$ [ET: bis(ethylenedithio)tetrathiafulvalene] by measuring optical second-harmonic generation (SHG), and discussed an electron-associated mechanism of the ferroelectric polarization based on the observation of ultrafast photo-modulation of the SHG.

This compound belongs to a series of radical-cationic complex with strongly correlated electrons. On account of D_2A chemical stoichiometry (D: donor, A: monovalent anion), donor molecules (ET) of the class of compounds receive one-half of positive charge from counterions ($2D + A \rightarrow 2D^{0.5+} + A^-$). It has been manifested however that some complexes including α-$(ET)_2I_3$ lost the mixed valency due to charge disproportionation ($2D^{0.5+} \rightarrow D^+ + D^0$) driven by repulsive Coulomb interactions between charges (Wigner crystallization).

The crystal of α-$(ET)_2I_3$ contains four ETs in the triclinic $P\bar{1}$ unit cell [Figure 1(a)]. There are two crystallographically independent stacks of ETs along the *a* axis; Stack I is a weakly dimerized chain composed of crystallographically equivalent ETs (labeled by *A* and *A*'), and Stack II is a uniform chain composed of *B* and *C*. According to an expected pattern of charge ordering, charges, which are delocalized in the metallic phase [Figure 1(a)], are localized to form such a pattern as illustrated in Figure 1(b) by the charge ordering. Since the equivalence between *A* and *A*' is broken in this pattern, the unit cell should possess a finite electrical dipole moment.

For most materials, electrical fields of those dipoles are cancelled out by the formation of an antiparallel dipole pair. However, we discovered that this complex exhibits SHG signal when it undergoes a metal-to-insulator transition due to charge ordering, manifesting that the transition is ferroelectric one, *i. e.*, local dipole moments are ordered in a polar arrangement to generate macroscopic polarization.

To examine the dynamic properties of the permanent polarization, we performed femtosecond pump-and-probe measurements of SHG; a crystal of the complex in ferroelectric state (T = 100 K) was stimulated by a pumping pulse, then

induced variation of SHG was recorded with a probing pulse. Figure 2 shows the evolution of the photoinduced variation of SHG observed. The profile demonstrates the very fast photo-response of the permanent polarization. The SHG signal instantly loses a large part of its intensity on pumping with the femtosecond pulse. Afterwards, it recovers to its original magnitude in the picosecond regime.

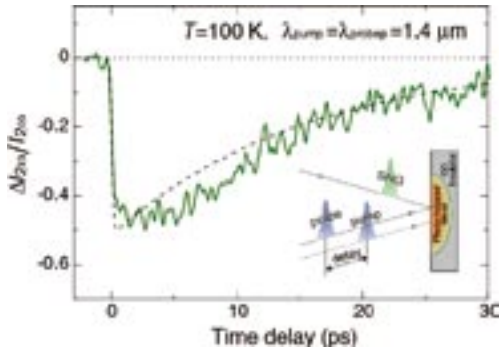

Figure 2. Photoinduced variation of SHG intensity as a function of the delay time between pump ($E||b$, 100 μJ/cm^2) and probe ($E||a$, 5 μJ/cm^2) pulses. The sample temperature was 100 K. The dashed line shows the fitted curve of single exponential decay (τ = 15 ps). The inset illustrates the pulse sequence of the time-resolved measurements.

Polarization in conventional ferroelectrics is attributed to a lattice modulation, such as polar displacement of ions, whereas one can hardly explain such fast photo-response of SHG with such a crystal lattice modulation. The substantially fast response illustrates that the ferroelectric polarization is modulated via a pure electronic process. It would be sure that the polarization is essentially attributed to the displacement of electrons due to the charge ordering.

Such electron-associated ferroelectrics are being recognized as a distinct class of the polar dielectrics. We believe that fast response of the polarization to external perturbations is one important characteristic of the new ferroelectrics, which may help to solve the problem in applying the controllable polarization to optoelectronic devices.

2. Inhomogeneous Site Charges at the Boundary between the Insulating, Superconducting, and Metallic Phases of β"-Type bis-ethylenedithio-tetrathiafulvalene Molecular Charge-Transfer Salts[2)]

β"-type ET salt involves rich superconducting compounds with the absence of strong dimerization. This family is possibly the good candidate for the charge-mediated superconducting transition, which is predicted by Merion and McKenzie. Some compounds in this family exhibits superconducting transition from an insulating ($d\rho/dT < 0$) state. We examined time-averaged charges on ET molecules around the phase boundary between the insulating, superconducting, and metal phases of β"-type ET salts with one hole per two molecules and two holes per three molecules by means of vibrational spectroscopy. We found that around the phase boundary, the site charges are neither those expected for a well-developed charge-ordered sate nor a uniform metallic state. The charge distribution is slightly inhomogeneous just above the insulator-superconductor phase transition temperature. We analyzed the distribution of the site charges from the viewpoint of the alternation of the strongest intersite Coulomb interaction along the stacking direction. The degenerate energy of several charge-ordered configuration generates a uniform state, the closeness in the energy of several charge-ordering configuration mostly contributes to the slight inhomogeneous distribution, and a large difference in their energy levels contributes to the charge ordered state. Our observation indicates that the instability due to the closeness in the energy of several configurations correlates with the insulator-superconductor transition in nondimerized or weakly dimerized molecular conductors.

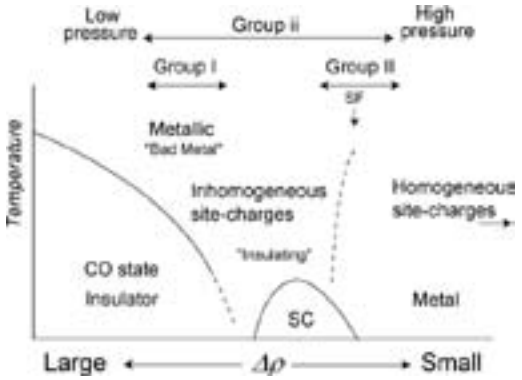

Figure 3. Schematic phase diagram of the β"-type ET salts plotted against the amplitude ($\Delta\rho$) of charge density wave. "SF" denotes β"-$(ET)_2SF_5CH_2CF_2SO_3$. The superconducting phase appears when $\Delta\rho \neq 0$.

References

1) K. Yamamoto, *et al.*, *J. Phys. Soc. Jpn.* **77**, 074709 (2008).
2) T. Yamamoto, *et al.*, *Phys. Rev. B* **77**, 205120 (2008).

Award

YAMAMOTO, Kaoru; Outstanding Poster Preasentation Prize, 7th International Symposium on Crystalline Organic Metals, Superconductors and Ferromagnets (ISCOM2007).

Magnetic Resonance Studies for Molecular-Based Conductors

Department of Materials Molecular Science
Division of Electronic Properties

NAKAMURA, Toshikazu	Associate Professor
FURUKAWA, Ko	Assistant Professor
IWASE, Fumitatsu	IMS Fellow
SUGIURA, Koichi	Graduate Student
ABE, Hitomi	Secretary

Magnetic resonance measurements are advantageous for studying fundamental electronic properties and for understanding the detailed electronic structures of molecular based compounds. Developing an understanding of the electronic phases and functionality of these materials enables us to perform systematic investigations of low-dimensional, highly-correlated electron systems and functional materials. Competition between the electronic phases in molecular-based conductors has attracted much attention.[1)] The investigations of such electronic phases by magnetic resonance measurements are important to understanding unsolved fundamental problems in the field of solid state physics, and to explore novel functionalities in the field of material science.

In this study, we performed broad-line NMR and ESR measurements on molecular-based conductors to understand electron spin dynamics and functionality in low-temperature electronic phases.

1. Another Commensurate Antiferromagnetic State in $(TMTTF)_2X$: ^{13}C NMR Investigation of $(TMTTF)_2SbF_6$

^{13}C nuclear magnetic resonance (NMR) investigations were performed on the one-dimensional organic conductor $(TMTTF)_2SbF_6$ to clarify its electronic properties in the proximity of the ground states. An abrupt broadening of ^{13}C NMR absorption lines below 8 K (T_N = 8 K), confirmed a long-range antiferromagnetic phase transition. Below T_N, the absorption lines are composed of four distinct broad lines.

The ^{13}C NMR spin-lattice relaxation rates, ^{13}C T_1^{-1}, for the distinct lines show critical enhancement just above T_N, and rapid decease below T_N. These observations indicate that the ground state of $(TMTTF)_2SbF_6$ is a commensurate antiferromagnetic phase. The amplitude of staggered magnetization, ρ, is comparable to $(TMTTF)_2Br$, and on the order of 0.1 μ_B, according to the splitting of ^{13}C NMR lines at 3 K. However the angular dependence of the ^{13}C NMR shifts shows slight differences between $(TMTTF)_2SbF_6$ and $(TMTTF)_2Br$.

2. ^{13}C NMR Study of the Chemical Pressure Effect in $(TMTTF)_2[(AsF_6)_x(SbF_6)_{1-x}]$ (x ~ 0.5), and Physical Pressure Effect for $(TMTTF)_2SbF_6$

Recently ISSP group discover superconductivity in $(TMTTF)_2SbF_6$ and $(TMTTF)_2AsF_6$ salts under ultra high pressures.[2,3)] If we remind the ground states of SbF_6 and AsF_6 are spin-Peierls (sP) and antiferromagnetic (AF), respectively, the so-called generalized phase diagram should be modified (AFI-sP-AFII). Curiously enough, the one-dimensional sP phase is sandwiched by two AF phases. And it is also an open question whether QCP is likely or unlikely. Hence, We performed ^{13}C NMR measurements for $(TMTTF)_2[(AsF_6)_x(SbF_6)_{1-x}]$ (x ~ 0.5) alloy, and $(TMTTF)_2SbF_6$ under pressure

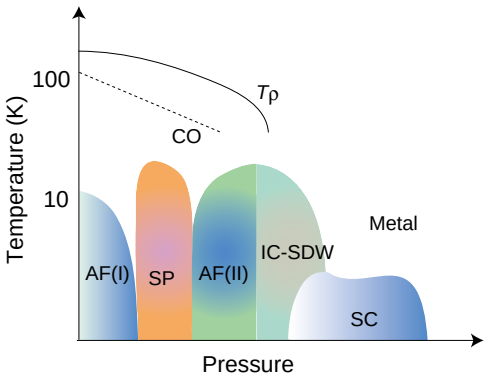

Figure 1. Modified generalized phase diagram for one-dimensional organic conductors, $(TMTCF)_2X$.

in order to clarify following issues: 1) Does Quantum Critical phenomena exist between the sP and AF Phase boundary? 2) Is the sP phase actually sandwiched by two AF phase? 3) Are AF-I and AF-II of the same origin or not?

As for $(TMTTF)_2[(AsF_6)_x(SbF_6)_{1-x}]$ (x ~ 0.5), the charge-order transition temperature is the intermediate value between the critical temperatures of SbF_6 and AsF_6. At low temperatures, we observed the characteristic behavior toward the

spin-Peierls phase transition. However, the temperature dependence of the spin-lattice relaxation rate is weak suggesting that this salt is situated in the vicinity of the phase boundary between the spin-Peierls and antiferromagnetic phases.

In the case of $(TMTTF)_2SbF_6$, we observed clear phase change from AF to sP under 5 kbar. This observation supports the modified generalized phase diagram.

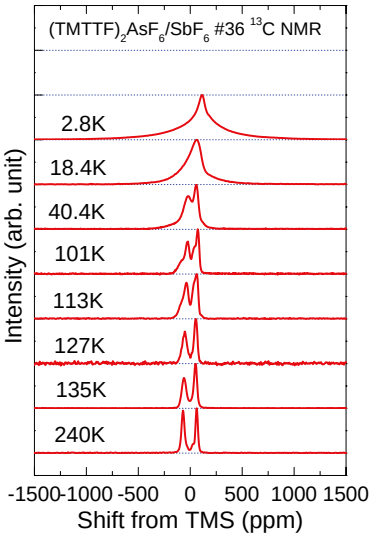

Figure 2. ^{13}C NMR spectra of $(TMTTF)_2[(AsF_6)_x(SbF_6)_{1-x}]$ ($x \sim 0.5$). The shift origin is TMS.

3. ESR Investigation of Novel Low-Dimensional Conductors, $(TMTTF)_2TaF_6$ and $(TMTTF)_3Ta_2F_{11}$

The electronic properties of one-dimensional organic conductor $(TMTTF)_2X$ were extremely investigated by a lot of researchers because of the variety of the electric properties. These electronic properties were drastically changed by external pressures or variety of counter anions (chemical pressure). In fact, the counter anion size is recognized as an important factor to emerge various type phases such as sP (spin-Peierls), SDW (spin density wave), CO (charge-order), AF (antiferromagnetic) and SC (superconductor).

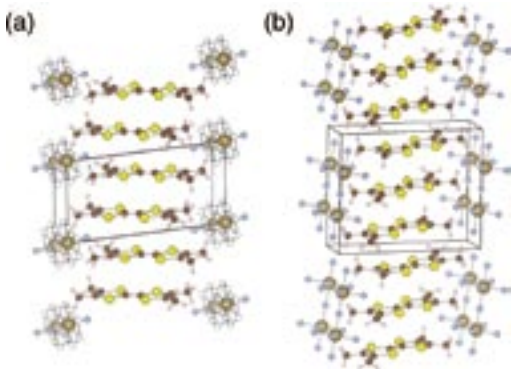

Figure 3. Crystal Structure of novel organic conductors, $(TMTTF)_2TaF_6$ and $(TMTTF)_3Ta_2F_{11}$.

Recently, we obtained novel organic conductors, $(TMTTF)_2TaF_6$ and $(TMTTF)_3Ta_2F_{11}$, by electrochemical oxidation. The lattice parameters of $(TMTTF)_2TaF_6$ are expected to be the largest among $(TMTTF)_2X$ family, and $(TMTTF)_2TaF_6$ is beyond the pristine Jérome phase diagram.[1] Hence, the electronic properties of $(TMTTF)_2TaF_6$ are not clarified and attracted much attention. It should be noted that the bandstructure of $(TMTTF)_3Ta_2F_{11}$ is different from those of typical organic conductors, $(TMTTF)_2X$ salts, since $(TMTTF)_3Ta_2F_{11}$ is a 3:1 salt. In this study, we carried out ESR measurements, and discuss the electronic states from the temperature dependence of the spin susceptibility, linewidth and g-value.

4. ESR Study of Spin Dynamics for Dye-Sensitized Solar Cell

In dye-sensitized solar cells (DSSC),[4] dye molecules are excited from the ground state S to the excited state S* by photo energy. The electron transfer from the excited dye molecules to the electrode plays an important role of the photoelectric transfer characteristic in DSSC. A various type of dye molecules were investigated. Time-resolved ESR measurements give us to detailed information of the photoelectric transfer characteristic. The aim of the present study is to reveal the relationship between the photoelectric transfer characteristic and the spin dynamics of electron in DSSC. The spin dynamics of the various organic dye molecules such as the eosin-Y was investigated by time-resolved ESR spectroscopy with laser photolysis (Nd:YAG 2nd harmonics, 532 nm). We discuss the spin dynamics of the various organic dye molecules with TiO_2.

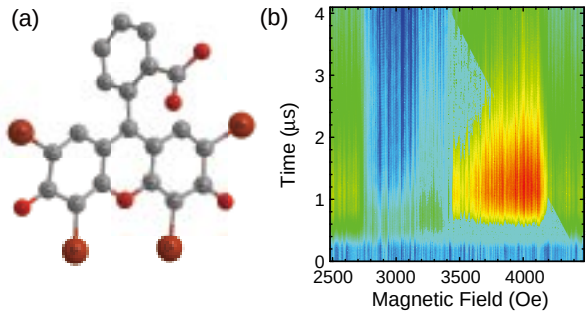

Figure 4. Molecular structure of eosin-Y, and time-resolved ESR spectroscopy of eosin-Y with laser photolysis.

References

1) for example: T. Ishiguro, K. Yamaji and G. Saito, *Organic Superconductors*, 2nd ed., Springer-Verlag; Berlin/Heidelberg (1998).
2) M. Itoi, M. Kano, N. Kurita, M. Hedo, Y. Uwatoko and T. Nakamura, *J. Phys. Soc. Jpn.* **76**, 053703 (5 pages) (2007).
3) M. Itoi, C. Araki, M. Hedo, Y. Uwatoko and T. Nakamura, *J. Phys. Soc. Jpn.* **77**, 023701 (4 pages) (2008).
4) B. O'regan and M. Gratzel, *Nature* **353**, 737 (1991).

Topological Design of Sheet-Shaped Macromolecules and Organic Framewarks

Department of Materials Molecular Science
Division of Molecular Functions

JIANG, Donglin	Associate Professor
ISHIZUKA, Tomoya	Assistant Professor
HE, Zheng	IMS Fellow
GUO, Jia	JSPS Post-Doctral Fellow
WAN, Shun	Graduate Student
CHEN, Long	Graduate Student
ODA, Masafumi	Graduate Student
YUSA, Masaaki	Graduate Student
ISONO, Yukiko	Technical Fellow
SUZUKI, Hiroko	Secretary

Covalent organic frameworks (COFs) are porous and crystalline macromolecules with a well-defined and predictable network of building blocks. Compared with inorganic porous materials, COFs are unique in that they are made from light elements, tunable in skeleton and robust against air and organic solvents. From synthetic point of view, COFs are attractive motifs since they allow, upon topological design, a total control over structure parameters including composition and porosity. Most studies up to date have focused on the development of synthetic methodologies with an aim to optimize pore size and surface area. By contrast, the functions of COFs except for gas storage have not yet been well explored. This motivated us to explore the possibility for constructing functional COFs with novel properties by utilizing highly ordered π-conjugation systems. We succeeded in the molecular design and synthesis of a series of novel COFs with unique semiconductive and photoconductive functionalities.

1. A Belt-Shaped, Blue Luminescent and Semiconductive Covalent Organic Framework

Herein, we report the first example of a luminescent and semiconductive COF, which adopts belt shape and consists of pyrene and triphenylene functionalities linked alternatively in a mesoporous hexagonal skeleton (Figure 1, TP-COF).

TP-COF was topologically designed by employing a D_{3h} symmetric monomer as corner and a D_{2h} symmetric monomer as edge for pore hexagons and synthesized by a condensation reaction of 2,3,6,7,10,11-hexahydroxytriphenylene (HHTP) and pyrene-2,7-diboronic acid (PDBA). FE SEM images of TP-COF reveal that the condensation polymerization of PDBA and HHTP afford belts with length extended to micrometers and width of about 300 nm and thickness of 100 nm. The belt morphology is quite uniform with a similar width and thickness to one another, and no other morphologies are observable. In high resolution TEM, clear aligned patterns were observed along the (110) facet. From the aligned layer structure, the distance between sheets is estimated to be 3.40 Å, which is reasonable for π-π stacking. Such a belt texture with a uniform morphology and the direct visualization of a stacked sheet structure are unprecedented for COFs. To our surprise, along the (001) facet, hexagonal mesostructure can be observed and enables the estimation of center-to-center distance between the neighboring pores to be about 3.3 nm. Powder x-ray diffraction (PXRD) exhibits a main diffraction peak due to 100 at 2.70°, along with diffractions owing to 110, 200, 210, 300, 310, and

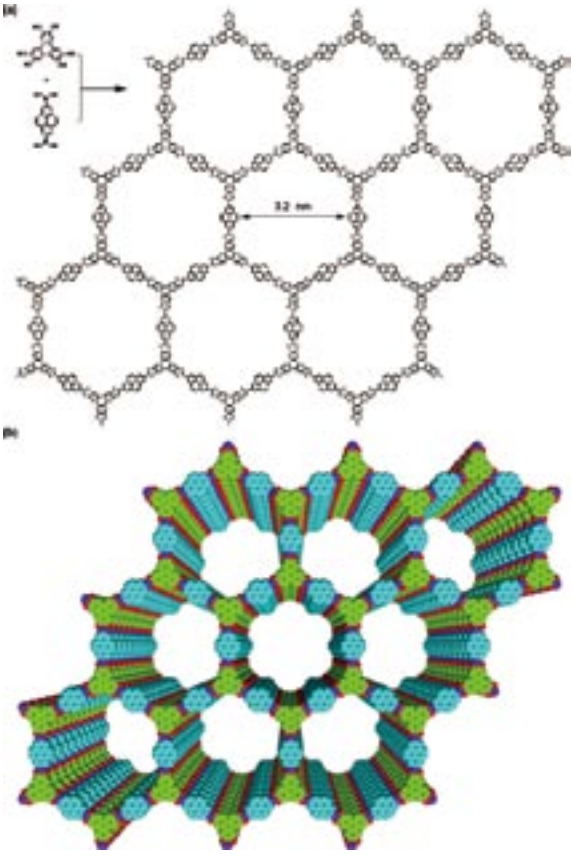

Figure 1. (a) Synthesis of TP-COF. (b) Schematic representation of TP-COF (Structure is based on quantum calculation and crystal lattice parameters; Purple: B, Red: O, Green: Triphenylene, Blue: Pyrene; H atoms are omitted for clarity).

001 at 4.74°, 5.46°, 7.26°, 8.24°, 9.54° and 26.32°, respectively. Simulation using the space group of *P*6/mmm (No. 191) with $a = b = 37.5412$ Å and $c = 3.3784$ Å gives a PXRD pattern in good agreement with the experimentally observed one. All the diffraction peaks can be reasonably assigned. Therefore, the 2-D sheets crystallize in an eclipsed fashion to give a perfect superimposition of the triphenylene and pyrene units on themselves. Such a crystalline structure would provide open and aligned mesopores of 3.26 nm in diameter. In fact, TP-COF exhibits a typical type IV nitrogen sorption curve, indicative of a mesoporous character (Figure 2). BET calculation gives specific surface area and pore volume of 868 $m^2 g^{-1}$ and 0.7907 $cm^3 g^{-1}$, respectively. Estimation of pore size with the DFT model shows a diameter of 3.14 nm, which is close to the theoretical one. Pore distribution profile shows that the specific surface area in TP-COF originates predominately from the persistent mesopores, whereas contributions of other pores formed between belts or from defects are small. All the above results indicate that TP-COF is a crystalline material with a uniformly sized mesopore formed via the eclipsed packing of the polymeric sheets.

Fluorescence microscopy exhibits that the belts of TP-COF are highly blue luminescent. Fluorescence spectroscopy shows that TP-COF emitted a luminescence at 474 nm, upon excitation of the pyrene units at 376 or 417 nm. Excitation of the triphenylene units in TP-COF at 340 nm resulted in negligibly weak emission at 402 nm from the triphenylene units but a strong emission from the pyrene moieties at 474 nm, where the fluorescence intensity ratio $I_{474\ nm}/I_{402\ nm}$ was as high as 16. In sharp contrast, when a 2:3 mixture of HHTP and PDBA was excited at 340 nm, it emitted predominately at 402 nm to furnish a low $I_{474\ nm}/I_{402\ nm}$ ratio (0.6). Therefore, the strong pyrene fluorescence, observed for TP-COF upon 340 nm excitation, is obviously due to an intramolecular singlet energy from the triphenylene units to pyrene units. Comparison of the excitation spectrum with diffuse reflectance UV-Vis spectrum, the quantum yield of energy transfer was estimated to be 60%. Therefore, by virtue of the triphenylene units, TP-COF can harvest photons of a wide wavelength range covering from ultraviolet to visible regions and converts them to blue emission. We further investigated the fluorescence anisotropy of TP-COF upon excitation with a polarized light. The 2:3 mixture of HHTP and PDBA shows a *p* value of 0.058. In sharp contrast, TP-COF under identical conditions exhibited a significantly depolarized fluorescence with an extremely low *p* value of 0.017. This observation reveals that TP-COF not only mediates energy transfer between components but facilitates energy migration over the crystalline belt as well.

Single crystals of pyrene and triphenylene have been reported to function as semiconductors. Due to the ultimate π-stacking of these large π-conjugated components, TP-COF

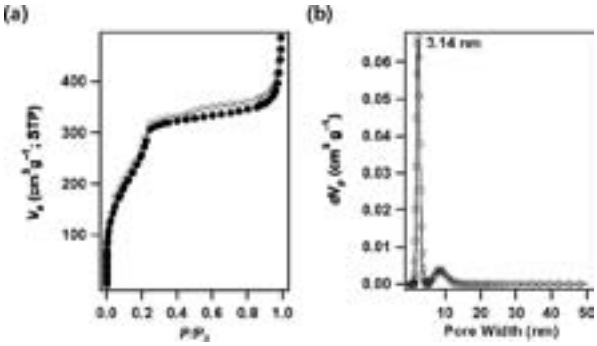

Figure 2. (a) Nitrogen adsorption (●) and desorption (○) isotherm profiles of TP-COF at 77 K. (b) Pore size distribution of TP-COF by DFT modeling on the N_2 adsorption isotherms.

may have a high probability of becoming electrically semiconductive. We investigated this possibility by measuring the electric conductivity with a 10-μm width Pt gap using a two-probe method. TP-COF in air at 25 °C shows an almost linear I-V profile, while the gap itself is silent irrespective of voltage bias. For example, at 2-V bais voltage, the electric current is 4.3 nA. In contrast, a 2:3 mixture of HHTP and PDBA shows a low current (79 pA) under otherwise identical conditions. Moreover, the electric current can be on/off switched repeatedly for many times without significant deterioration. The relatively high electric current observed for TP-COF is likely related to the highly order structure that enables the formation of a conductive path. Upon doping with iodine, the electric current was increased, suggesting a *p*-type semiconductor character of TP-COF.

Exploration of functional COFs is a subject with a high probability to the development of new materials. We have succeeded in the synthesis of a new COF based on the condensation reaction of triphenylene and pyrene monomers. TP-COF is highly luminescent, harvests a wide wavelength range of photons and allows energy transfer and migration. Furthermore, TP-COF is electrically conductive and capable of repetitive on-off current switching at room temperature. These characters are unique and clearly originate from the highly ordered structure of TP-COF. By filling the mesopores with photoactive molecules such as electron acceptor, we expect the fabrication of COF-based optoelectronic device, which is one of the targets under investigation.

Reference

1) S. Wan, J. Guo, J. Kim, H. Ihee and D. Jiang, *Angew. Chem., Int. Ed.* **47**, 8826–8830 (2008) (VIP, Selected as a frontispiece of ACIE).

2) Jyllian N. Kemsley, *C&EN* **86**, 29 (2008) (Highlight).

Award

CHEN, Long; Student Lecture Award of Chemical Society of Japan (2008).

Methodology Developments of Solid State NMR Spectroscopy for Structural Biology and Material Science

Department of Materials Molecular Science
Division of Molecular Functions

NISHIMURA, Katsuyuki — Associate Professor
IIJIMA, Takahiro — Assistant Professor
UEKAMA, Naoko — IMS Fellow

Solid state NMR is one of the useful tools to characterize dynamics and structures of molecules on amorphous condition without specific limitations. We are focusing on methodology developments of solid state NMR especially for structural biology and material science. We are also attempting to elucidate functions and dynamic structure of peripheral membrane protein bound to lipid bilayer surface based on solid state NMR. In the following, we show the newly developed techniques to enhance spectral resolution and sensitivity in solid state NMR spectroscopy, and a study of structural change depending on weak interaction between peripheral membrane protein and lipid bilayer surface.

1. Spectral Resolution Enhancements Based on Doubly Magnified Evolution of Internal Interaction in Solid State NMR[1)]

In order to enhance the spectral resolution of 2D correlation experiments in solid state NMR spectroscopy, general scheme enabling doubly magnified evolution of specific internal interaction was developed. The efficacy of this approach was verified by applying it to several conventional techniques. As first example, doubly magnified heteronuclear 2D J-spectroscopy under magic angle spinning (MAS) in solid was developed to enhance separation of multiplet signals due to heteronuclear J-coupling. J-couplings are very useful parameters in solution NMR for assignments of peaks and establishment of through bond connectivities. In solid-state NMR, however, J-couplings are less frequently observed because of their small amplitudes respect to the other interactions.

In conventional constant evolution time heteronuclear J-spectroscopy, heteronuclear J-coupling evolution takes place by replacement of heteronuclear decoupling sequence with multiple-pulse (MP) sequence removing ^{1}H homonuclear dipolar interaction under MAS. In contrast to the conventional technique, MP is applied to whole constant evolution time in newly developed one. Then, MPs are replaced by the ones exhibiting the same form of average Hamiltonian (AH) for heteronuclear J-coupling with opposite sign. As a result, the effective evolution becomes double and it gives doubled multiplets due to J-couplings in Hz unit without change of line width. Thus the spectral resolution can be improved by twice. Figure 1 (b) and (c) show the J-resolved spectra obtained from

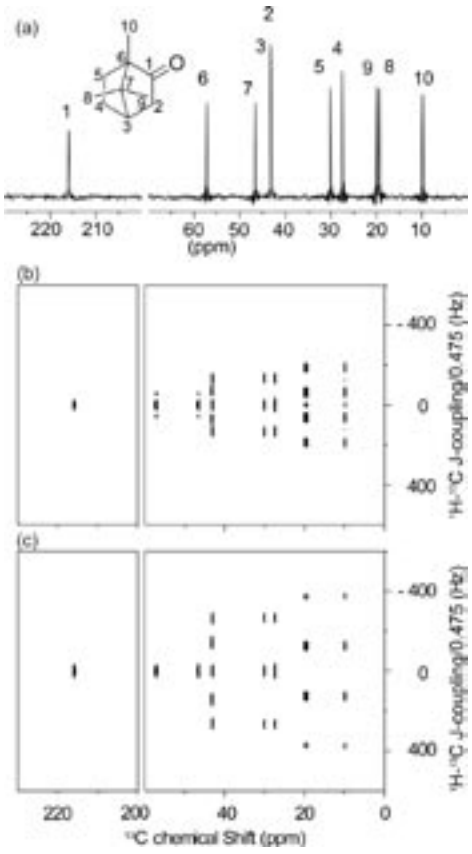

Figure 1. (a) 1D-CPMAS spectrum of Camphor. 2D J-resolved spectra of solid Camphor obtained from (b) conventional and (c) doubly magnified techniques under MAS, respectively. J-coupling axes are corrected by scaling factor of MP.

conventional and newly developed ones, respectively. It is important to note that no specific limitation over conventional technique exists to perform new experiment.

Similar idea can be applied for the measurements of heteronuclear dipolar interaction. That technique is effective especially to observe motionally averaged dipolar interaction in oriented sample.[2)]

2. QCPMG NMR of Spin-1 Nuclei in the Presence of Shift Interaction[3)]

Quadrupole Curr-Purcell-Meiboom-Gill (QCPMG) sequence is an efficient method to enhance NMR signals of quadrupole nuclei with acquisition of successive echo signals generated by refocusing pulses. QCPMG sequence that can be combined with other solid-state NMR techniques such as magic angle spinning, multiple quantum/magic angle spinning and double frequency sweep has been widely utilized for structural investigation of materials possessing quadrupole nuclei. However, it has been recently reported that QCPMG is inefficient in the presence of a shift interaction for spin-1 nuclei including ^{2}H and ^{14}N, and application of QCPMG of such nuclei for structural study has been limited.

In this work, we developed improved QCPMG technique for spin-1 nuclei that can obtain an in-phase spectrum under the influence both of the quadrupole and shift interactions. Essences of the present method are (i) addition of radio-frequency (RF) pulses that only affect the refocusing of the shift interaction and (ii) an irradiation of a strong RF field to prevent a signal arising from unwanted coherence pathways.

Figure 2 shows comparison of ^{2}H NMR spectra for a model compound of $CoSiF_6 \cdot 6H_2O$ obtained from conventional and improved QCPMG methods. It is known that a paramagnetic shift interaction between ^{2}H nuclei and electron spins in Co^{2+} ion in addition to the quadrupole interaction contributes to the ^{2}H NMR spectrum of this sample. Since the former interaction is considerably large (> 30 kHz), application of conventional QCPMG pulse sequence results in a phase distorted spectrum as shown in Figure 2 (a). Figure 2 (b) is the QCPMG spectrum obtained from improved QCPMG pulse sequence with the RF field of 210 kHz. As expected, the spectrum is free from distortion. Thus, NMR parameters can be obtained by comparison with simulated one as shown in Figure 2 (c).

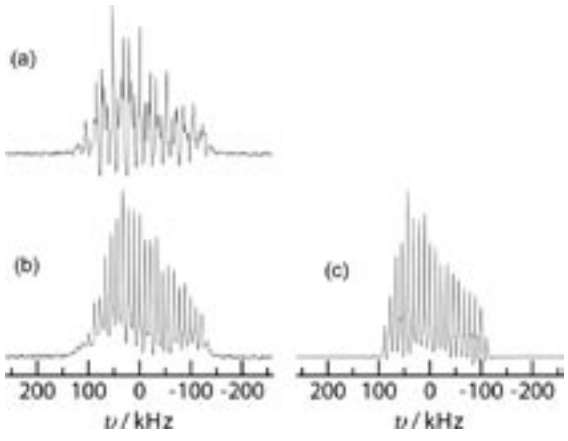

Figure 2. ^{2}H (I = 1) QCPMG NMR spectrum of $CoSiF_6 \cdot 6H_2O$ at 61.385 MHz. (a) and (b) show the spectra obtained by the conventional and improved QCPMG methods, respectively. (c) The simulated spectrum for improved QCPMG.

3. Influence of Membrane Curvature on the Structure of the Membrane-Associated Pleckstrin Homology Domain of Phospholipase C-δ1[4)]

Phospholipase C-δ1 (PLC-δ1) hydrolyzes phosphatidylinositol 4, 5-bisphosphate (PIP_2) in the plasma membrane to produce the second messengers on the membrane surface. The PH domain in the N-terminus of PLC-δ1 selectively forms high affinity complex with PIP_2 in the plasma membrane and IP_3 in the cytoplasm. Consequently those complex formations regulate membrane localization of PLC-δ1. From the previous studies, it is known that α2-helix is responsible for auxiliary membrane binding site in addition to the PIP_2 specific membrane binding site and the terminous of β5/β6 loop plays a role of hinge connecting the β-sandwich core of the PH domain.

In this study, conformational changes of the PLC-δ1 PH domain bound to the surfaces of multilamellar vesicles (MLVs), small unilamellar vesicles (SUVs), and micelles were investigated to evaluate the effects of membrane curvatures on the membrane-associated protein based on solid-state NMR spectroscopy. The conformational changes of PLC-δ1 PH domain bound to those surfaces were evaluated from the analyses of conformational dependent ^{13}C isotropic chemical shifts of isotope enriched [3-^{13}C] Ala sites in PH domain. As results, ^{13}C NMR signals of Ala88 in the α2-helix and Ala112 spatially close to the terminus of the β5/β6 loop containing the α2-helix exhibited conformational changes due to the reorientation of the α2-helix on the surface of MLV and SUV membrane. In contrast, no conformational change of those regions was observed on the surfaces of the DPC and DM micelles with diameter of 33–40 Å. According to those results, we found out that the terminus of β5/β6 loop is susceptible to the alteration of the curvature of lipid bilayer surface, and the mutual orientation of two membrane binding sites of the PH domain on the curved membrane.

It is known that the membranes in the cell undergo dynamic alterations of their structures and their chemical composition during the physiological processes. Those induce time dependence of local curvature of membrane. Thus the conformational changes of the membrane binding domain such as found in this study for the PLC-δ1 PH domain may affect the membrane binding mechanism of peripheral membrane proteins.

References

1) K. Nishimura, submitted.
2) K. Nishimura, to be submitted.
3) T. Iijima and K. Nishimura, to be submitted.
4) N. Uekama, T. Aoki, T. Maruoka, S. Kurisu, A. Hatakeyama, M. Okada, H. Yagisawa, K. Nishimura and S. Tuzi, submitted.

Organic Solar Cells

Research Center for Molecular Scale Nanoscience
Division of Molecular Nanoscience

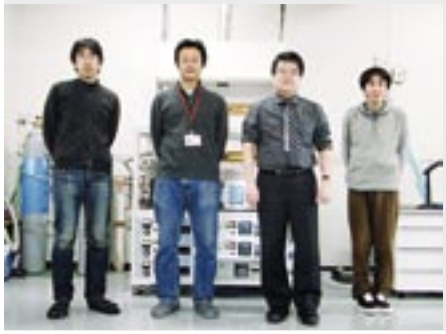

HIRAMOTO, Masahiro	Professor
IKETAKI, Kai	IMS Fellow
NAKAO, Satoru	Post-Doctoral Fellow
KITADA, Keitaro	Graduate Student*
PFÜTZNER, Steffen	Graduate Student†
SUZUKI, Hiroko	Secretary

Organic EL television was commercialized last year. Next target of organic electronics is organic solar cell. Our group accomplished the world record conversion efficiency of 5.3% based on the fundamental research on the organic semiconductors such as ultra-high purification, nanostructure design. Moreover, 1000 h (42 days) operation of organic solar cell without degradation was accomplished.

1. Efficient Organic *p-i-n* Solar Cells Having 1 μm-Thick Codeposited *i*-Layer Incorporating Seven-Nine (7N) Purified Fullerene[1)]

In 1991, we proposed *p-i-n* organic solar cells in which the *i*-interlayer is a codeposited film composed of *p*- and *n*-type organic semiconductors.[2,3)] Since *i*-interlayer acts as an efficient photocarrier generation layer, if this codeposited *i*-interlayer could be thick enough to be able to absorb entire irradiated solar light, organic *p-i-n* cells would show the magnitude of photocurrent density comparable to inorganic solar cells.

Unfortunately, *i*-interlayer has been inevitably very thin. For example, we have reported *p-i-n* organic solar cells in which the *i*-interlayer is nanostructure-optimized codepostied film composed of fullerene and metal-free phthalocyanine (C_{60}:H_2Pc).[4)] At that time, thickness of C_{60}:H_2Pc *i*-interlayer was limited below 180 nm since the fill factor (FF) was seriously decreased for thicker *i*-interlayer due to the increase of internal resistance of *i*-layer.

On the analogy of the case of Si which is usually purified to eleven-nine (11N), we convinced that the purity of organic semiconductors should be reached to ppm level at least in order to draw out their essential nature.

In this study, we performed the single-crystal formed sublimation under N_2 gas of 1 atm (Figure 1). Due to the gas convection, in the case of C_{60}, single crystals of the maximum size of 2 mm × 2 mm were obtained (Figure 2). C_{60} purity was determined by the secondary ion mass spectroscopy (SIMS), which has been used for the analysis of dopants in Si wafer. Purity of C_{60} crystals purified three times was more than 0.1 ppm, *i.e.*, seven-nine (7N). On the other hand, purity of H_2Pc sample purified four times was five-nine (5N).

Figure 1. Photograph of single-crystal formed sublimation apparatus.

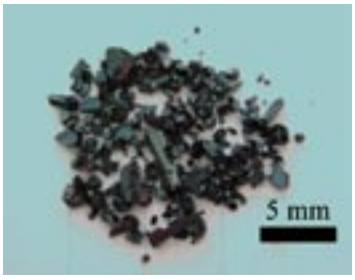

Figure 2. Photograph of C_{60} single crystals. Crystal size reached 2 mm × 2 mm.

p-i-n cell structure is shown in Figure 4. *p*-type layer of H_2Pc, codeposited *i*-interlayer composed of C_{60} and H_2Pc, and *n*-type layer of NTCDA, which also acts as a transparent protection layer, were successively deposited by vacuum evaporation on ITO glass substrate. Codeposited films were fabricated by the coevaporation from two separately controlled sources on the substrate heated at +80 °C.

Figure 3(a) shows the dependence of fill factor (FF) on *i*-interlayer thicknesses (*X*). Surprisingly, FF hardly decreased

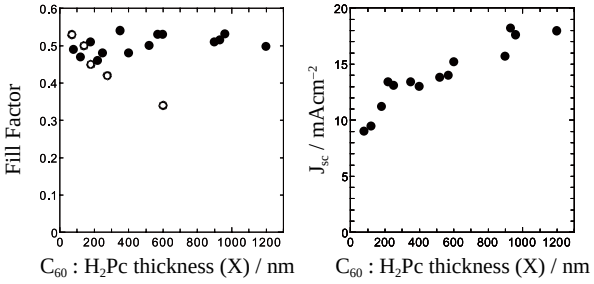

Figure 3. Dependence of fill factor (FF) and short-circuit photocurrent (J_{sc}) on *i*-interlayer thickness (X) for organic *p*-*i*-*n* cells.

even for very thick *i*-layer reaching 1.2 μm (closed dots). Accordingly, short-circuit photocurrent density (J_{sc}) increased with X and reached maximum value of 19.1 mAcm^{-2} at X = 1 μm (Figure 3(b)). When we used C_{60} of low-purity by the conventional sublimation under vacuum, FF monotonically decreased with X and, as a result, thick *i*-layer could not be fabricated (Figure 3(a), open dots).

Figure 4 shows the current-voltage (J-V) characteristics for *p*-*i*-*n* cell having 1 μm-thick *i*-interlayer. J_{sc} of 18.3 mAcm^{-2}, open-circuit photovoltage (V_{oc}) of 0.402 V, FF of 0.532, and conversion efficiency 5.3% were observed.

Since the present cell (X = 1 μm) absorbs whole visible light, cell color is black (Figure 5(a)). On the contrary, cell having thin *i*-layer (X = 180 nm), cell color is transparent green (Figure 5(b)), namely, large portion of irradiated light can not be utilized. Utilization of entire visible light of solar spectrum without decreasing FF by incorporating very thick C_{60}:H_2Pc *i*-interlayer is essential to obtain large J_{sc} value close to 20 mAcm^{-2} and efficiency of 5.3%.

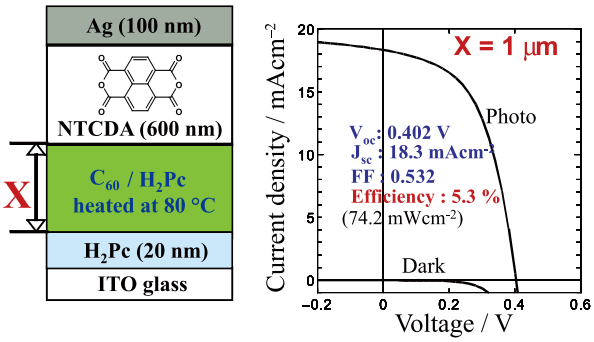

Figure 4. Cell structure and current-voltage (J-V) characteristics for *p*-*i*-*n* cell having 1 μm-thick *i*-layer.

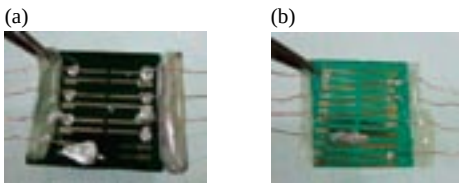

Figure 5. Photographs of cells. (a) X = 1 μm. (b) X = 180 nm.

2. Long-Term Operation for 42 Days

The conversion efficiency of organic solar cells is expected to exceed the practical level (10%) within few years. However, few studies have been made on their durability.[5)]

In this study, we performed the long-term operation tests reaching 1000 h in high vacuum (10^{-7} Torr). White light (100 mWcm^{-2}) was continuously irradiated under the short-circuit condition. Gradual degradation within 100 h was observed for *p*-*i*-*n* cells having the structure of Figure 4. Detailed investigation revealed that the photodegradation of NTCDA, which acts as the transparent *n*-type layer, occurred.

Therefore, we replaced NTCDA with Al-doped ZnO (AZO) fabricated by electron beam evaporation on organic film (Figure 6). Fabricated AZO was transparent and showed the conductivity of 10^3 Scm^{-1}, which is comparable to ITO. Little decrease of J_{sc} and efficiency after 1000 h operation was confirmed (Figure 6). This is good news for the practical application of organic solar cells.

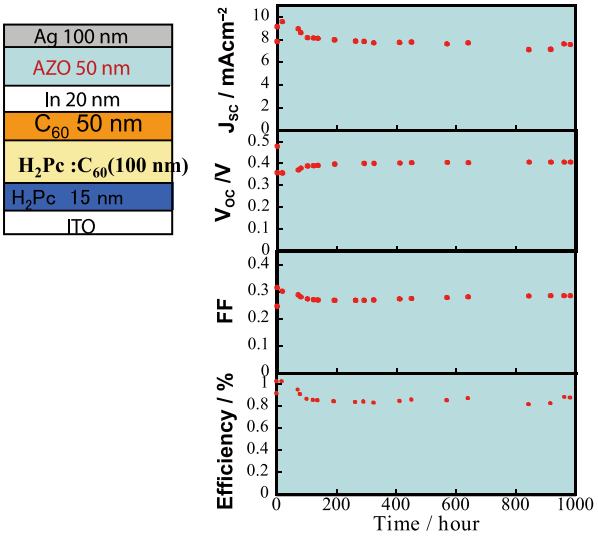

Figure 6. Cell parameters *vs.* operating time for a cell incorporating transparent AZO layer.

References

1) M. Hiramoto, *Proc. SPIE Vol. 7052, Organic photovoltaics IX* pp. 70520H-1–6, San Diego, CA, 12-14 Aug. (2008).
2) M. Hiramoto, H. Fujiwara and M. Yokoyama, *J. Appl. Phys.* **72**, 3781 (1992).
3) M. Hiramoto, H. Fujiwara and M. Yokoyama, *Appl. Phys. Lett.* **58**, 1062 (1991).
4) K. Suemori, T. Miyata, M. Yokoyama and M. Hiramoto, *Appl. Phys. Lett.* **86**, 063509 (2005).
5) H. Shiokawa, M. Yokoyama and M. Hiramoto, *Surf. Rev. Lett.* **14**, 539–542 (2007).

* carrying out graduate research on Cooperative Education Program of IMS with Osaka University
† from Technische Universität Dresden

Development of Organic Semiconductors for Molecular Thin-Film Devices

Research Center for Molecular Scale Nanoscience
Division of Molecular Nanoscience

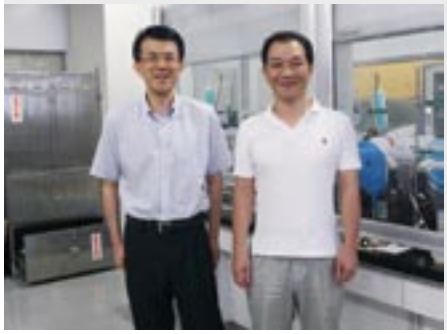

SUZUKI, Toshiyasu	Associate Professor
SAKAMOTO, Youichi	Assistant Professor
OKUBO, Kimitaka	Graduate Student
WATANABE, Yoko	Secretary

Organic light-emitting diodes (OLEDs) and organic field-effect transistors (OFETs) based on π-conjugated oligomers have been extensively studied as molecular thin-film devices. Organic semiconductors with low injection barriers and high mobilities are required for highly efficient OLEDs and OFETs. Radical cations or anions of an organic semiconductor have to be generated easily at the interface with an electrode (or a dielectric), and holes or electrons must move fast in the semiconducting layer. Compared with organic p-type semiconductors, organic n-type semiconductors for practical use are few and rather difficult to develop. Recently, we found that perfluorinated aromatic compounds are efficient n-type semiconductors for OLEDs and OFETs.

1. Synthesis, Structure, and Transport Property of Perfluorinated Oligofluorenes[1)]

We report the synthesis, structure, and properties of perfluorinated oligo(9,9-dimethylfluorene)s (**PF-*n*F**s). The cyclic voltammetry of **PF-3F** and **PF-4F** showed two reversible couples in THF. The reduction potentials are much more positive than those of conventional electron transport materials. **PF-3F** and **PF-4F** exhibited high glass transition temperatures (T_g = 133 and 163 °C, respectively), indicating that they are highly stable amorphous solids. The X-ray crystallography of **PF-2F** showed that a single crystal contained a 1:1 mixture of *cis* and *trans* conformers. The electron mobilities were measured by the time-of-flight technique. **PF-3F** and **PF-4F** displayed weak field dependence and high electron mobilities as amorphous n-type semiconductors (2.1×10^{-4} and 2.0×10^{-4} cm^2 V^{-1} s^{-1} at 6×10^5 V cm^{-1}, respectively).

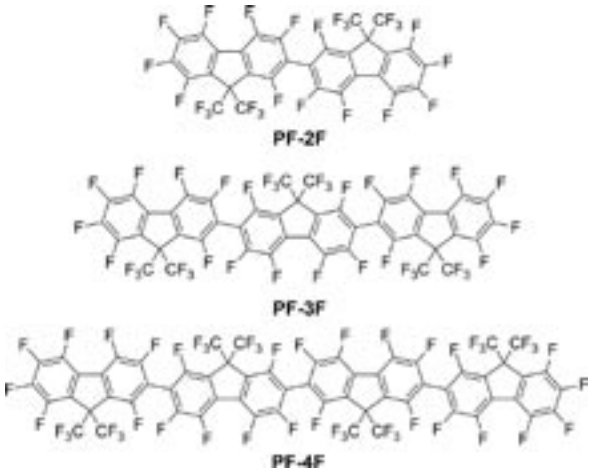

Figure 1. Structures of perfluorinated oligo(9,9-dimethylfluorene)s.

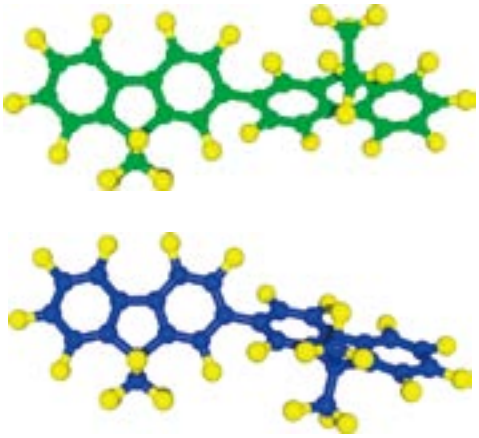

Figure 2. X-ray structures of *trans*-**PF-2F** (top) and *cis*-**PF-2F** (bottom).

2. Optical Properties of Pentacene and Perfluoropentacene Thin Films[2)]

The optical properties of pentacene (PEN) and perfluoropentacene (PFP) thin films on various SiO_2 substrates were studied using variable angle spectroscopic ellipsometry. Structural characterization was performed using x-ray reflectivity and atomic force microscopy. A uniaxial model with the optic axis normal to the sample surface was used to analyze the ellipsometry data. A strong optical anisotropy was observed, and enabled the direction of the transition dipole of the absorption bands to be determined. Furthermore, comparison of the optical constants of PEN and PFP thin films with the absorption spectra of the monomers in solution shows significant changes due to the crystalline environment. Relative to the monomer spectrum, the highest occupied molecular orbital to lowest unoccupied molecular orbital transition observed in PEN (PFP) thin film is reduced by 210 meV (280 meV). A second absorption band in the PFP thin film shows a slight blueshift (40 meV) compared to the spectrum of the monomer with its transition dipole perpendicular to that of the first absorption band.

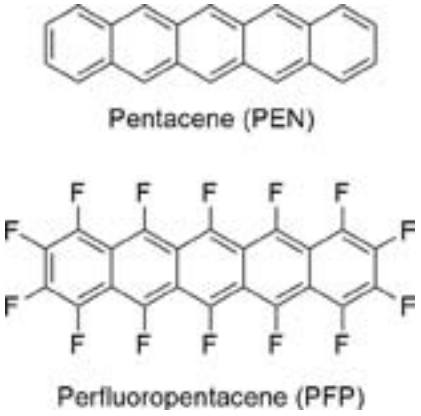

Figure 3. Structures of pentacene (PEN) and perfluoropentacene (PFP).

3. Adsorption-Induced Intramolecular Dipole: Correlating Molecular Conformation and Interface Electronic Structure[3)]

The interfaces formed between pentacene (PEN) and perfluoropentacene (PFP) molecules and Cu(111) were studied using photoelectron spectroscopy, X-ray standing wave (XSW), and scanning tunneling microscopy measurements, in conjunction with theoretical modeling. The average carbon bonding distances for PEN and PFP differ strongly, that is, 2.34 Å for PEN versus 2.98 Å for PFP. An adsorption-induced nonplanar conformation of PFP is suggested by XSW (F atoms 0.1 Å above the carbon plane), which causes an intramolecular dipole of ~0.5 D. These observations explain why the hole injection barriers at both molecule/metal interfaces are comparable (1.10 eV for PEN and 1.35 eV for PFP) whereas the molecular ionization energies differ significantly (5.00 eV for PEN and 5.85 eV for PFP). Our results show that the hypothesis of charge injection barrier tuning at organic/metal interfaces by adjusting the ionization energy of molecules is not always readily applicable.

4. TStructural Order in Perfluoropentacene Thin Films and Heterostructures with Pentacene[4)]

Synchrotron X-ray diffraction reciprocal space mapping was performed on perfluoropentacene (PFP) thin films on SiO_2 in order to determine the crystal structure of a novel, substrate-induced thin film phase to be monoclinic with unit cell parameters of a = 15.76 ± 0.02 Å, b = 4.51 ± 0.02 Å, c = 11.48 ± 0.02 Å, and β = 90.4 ± 0.1°. Moreover, layered and co-deposited heterostructures of PFP and pentacene (PEN) were investigated by specular and grazing-incidence X-ray diffraction, atomic force microscopy, and Fourier-transform infrared spectroscopy. For a ca. three-monolayers-thick PFP film grown on a PEN underlayer, slightly increased lattice spacing was found. In contrast, co-deposited PEN/PFP films form a new mixed-crystal structure with no detectable degree of phase separation. These results highlight the structural complexity of these technically relevant molecular heterojunctions for use in organic electronics.

References

1) K. Ohkubo, Y. Sakamoto, T. Suzuki, T. Tsuzuki, D. Kumaki and S. Tokito, *Chem. Eur. J.* **14**, 4472–4474 (2008).
2) A. Hinderhofer, U. Heinemeyer, A. Gerlach, S. Kowarik, R. M. J. Jacobs, Y. Sakamoto, T. Suzuki and F. Schreiber, *J. Chem. Phys.* **127**, 194705 (6 pages) (2007).
3) N. Koch, A. Gerlach, S. Duhm, H. Glowatzki, G. Heimel, A. Vollmer, Y. Sakamoto, T. Suzuki, J. Zegenhagen, J. P. Rabe and F. Schreiber, *J. Am. Chem. Soc.* **130**, 7300–7304 (2008).
4) I. Salzmann, S. Duhm, G. Heimel, J. P. Rabe, N. Koch, M. Oehzelt, Y. Sakamoto and T. Suzuki, *Langmuir* **24**, 7294–7298 (2008).

Building Photosynthesis by Artificial Molecules

Research Center for Molecular Scale Nanoscience
Division of Molecular Nanoscience

NAGATA, Toshi	Associate Professor
NAGASAWA, Takayuki	Assistant Professor*
KON, Hiroki	IMS Fellow
ALLAKHVERDIEV, Suleyman I.	Visiting Scientist; JSPS Invited Fellow†
KAWAO, Masahiro	JSPS Post-Doctoral Fellow
TANEMURA, Hiroyo	Technical Fellow
WANATABE, Yoko	Secretary

The purpose of this project is to build nanomolecular machinery for photosynthesis by use of artificial molecules. The world's most successful molecular machinery for photosynthesis is that of green plants—the two photosystems and related protein complexes. These are composed almost exclusively from organic molecules, plus a small amount of metal elements playing important roles. Inspired by these natural systems, we are trying to build up multimolecular systems that are capable of light-to-chemical energy conversion. At present, our interest is mainly focused on constructing necessary molecular parts.

1. Synthesis of Porphyrin-Cyclopentadienylcobalt(III) Linked Molecules

The light reactions of oxygenic photosynthesis produce dioxygen and NADPH by the aid of photon energy. Although the actual mechanism is very complicated, the net reaction can be conceptually outlined into three unit reactions; the initial photoinduced electron transfer, and the oxidizing and reducing reactions at the both ends of the charge separated state. In this context, the combination of photoinduced electron transfer and a redox reaction mediated by metal complexes is an interesting subject. One interesting target is the redox chemistry of cyclop entadienylcobalt(III) (CpCo) complexes,[1)] which are known to catalyze various redox reactions, including production of hydrogen. However, photoinduced electron transfer from organic pigments like porphyrins to CpCo complexes is not so easy to achieve.

In this work, we report the synthesis of new dyad molecules, **1** and **2**, which contain porphyrin and cyclopentadienyl cobalt(III) (CpCo) moieties within one molecule. The fluorescence emission spectra showed that the singlet excited state of the porphyrin was quenched via intramolecular electron transfer to the CpCo moiety.

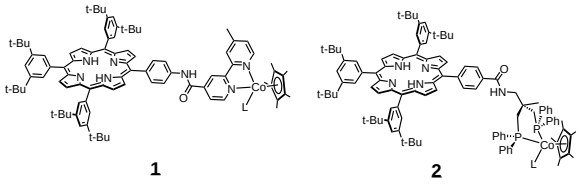

Figure 1. The porphyrin-CpCo linked compounds.

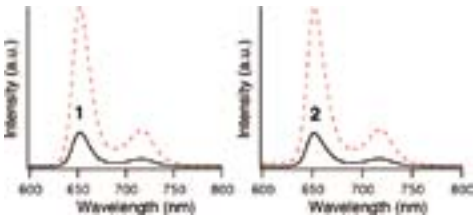

Figure 2. The steady-state emission spectra of compounds **1** and **2** in CH_2Cl_2. The red dotted lines indicate the emission spectra of the reference compound without the CpCo moiety.

2. An Approach towards Artificial Quinone Pools: Alcohols as the Terminal Reductant[2)]

Quinones are one of the most important cofactors in biological photosynthesis. In the "Type-II" photosynthetic reaction centers, quinones are the terminal electron acceptors, which receive electrons from the photoexcited chlorophylls and are converted into quinols. The quinols are released from the reaction center into the quinone pool, and are eventually reoxidized with concurrent translocation of protons through the membrane. Such a characteristic of natural quinone pools is worth mimicking in artificial systems, because it will provide a key to realize the "Z-scheme" in artificial photosynthesis.

The ultimate goal in mimicking the quinone pools is to convert quinones to quinols with concurrent oxidation of water. However, this is a difficult objective, so we are looking for other oxidation reactions that can be easily realized and can be combined with conversion of quinones to quinols.

In this work, we study the combination of a photoinduced electron tranfer from the porphyrin to the quinone and a TEMPO-catalyzed oxidation of alcohols triggered by one electron oxidation (eq. 1). The dependence of initial rates on the oxidation potentials of the porphyrin showed a characteristic bell shape, which is caused by two competitive factors, the efficiency of photoinduced electron transfer and the equilibrium of electron exchange between the porphyrin cation radical and TEMPO.

$$RCH_2OH + Q \xrightarrow[\text{[porphyrin]}]{h\nu} RCHO + QH_2 \quad (1)$$

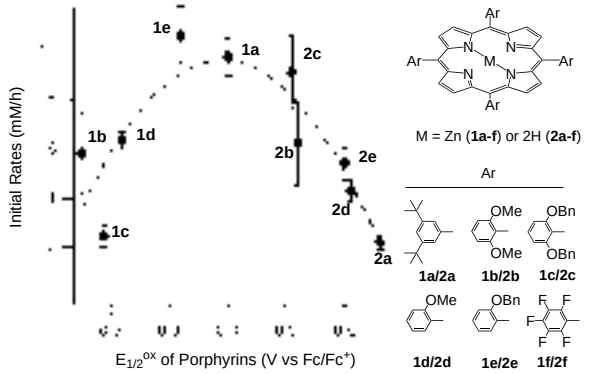

Figure 3. The initial rates of formation of PhCHO plotted versus the oxidation potentials of the porphyrins.

3. Reconstitution of the Water-Oxidizing Complex in Photosystem II Using Synthetic Mn Complexes: A Fluorine-19 NMR Study[3)]

Oxygen evolution is one of the most important processes in plant photosynthesis. The function is performed at the oxygen-evolving complex (OEC), which resides at the oxidizing terminal of Photosystem II (PS2) and contains manganese ions as essential cofactors. One interesting approach research on photosynthetic oxygen evolution is the reconstitution of the Mn-depleted PS2 with synthetic Mn complexes. In some cases the reconstituted PS2 shows similar activity as the native one, and in other cases the reconstituted PS2 performs different reaction from the native one.[4)] However, owing to the large size and extreme complexity of the PS2 protein, it is not easy to elucidate the reconstitution process at the molecular level. Specifically, the fate of the synthetic ligands during the reconstitution process remained unclear.

In this work, we developed a new tricarboxylate ligand **1** containing fluorine (Figure 4). The ligand is designed suitably to bind to a trinuclear $Mn_3(\mu_3\text{-O})$ core, which is an important structural motif in the OEC. When the Mn-depleted PS2 particles were treated with the trinuclear Mn complex **2**, all the photosynthetic activities (including oxygen evolution) were restored. It was particularly notable that the reconstitution was completed at much lower concentration than the simple salts like $MnCl_2$, which suggests the positive role of the ligand in the reconstitution process.

The ^{19}F NMR of the reconstituted PS2 was examined. In spite of the very low concentration of the Mn complex, the signal was clearly observed after 30000 scans (Figure 5). This signal was assigned to the free ligand **1**, which indicates that the ligand was released from the complex **2** during the reconstitution. On the other hand, in the absence of the PS2 particles the decomposition of the complex **2** was slow. We propose that the primary step in the reconstitution process is the prebinding of the Mn complex to the hydrophobic part of the PS2 particle. This proposal is also consistent with our previous results on the reconstitution of OEC with synthetic Mn complexes.

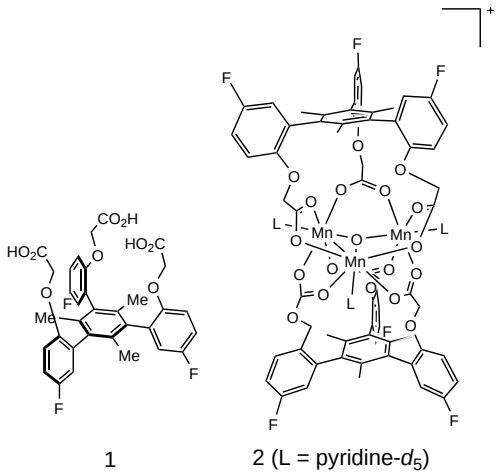

Figure 4. The tricarboxylate ligand **1** and the Mn_3 complex **2**.

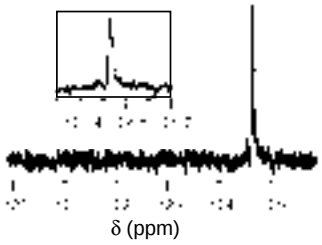

Figure 5. ^{19}F NMR spectra of the mixture of the Mn-depleted PSII particles (Chl 100 mg ml^{-1}) and **2** (10 μM) in the MES/D_2O buffer.

References

1) T. Nagasawa and T. Nagata, *Biochim. Biophys. Acta* **1767**, 666–670 (2007).

2) T. Nagasawa, S. I. Allakhverdiev, Y. Kimura and T. Nagata, *Photochem. Photobiol. Sci.* in press. (DOI: 10.1039/b815101f)

3) T. Nagata, S. K. Zharmukhamedov, A. A. Khorobrykh, V. V. Klimov and S. I. Allakhverdiev, *Photosynth. Res.* in press. (DOI: 10.1007/s11120-008-9319-9)

4) T. Nagata, T. Nagasawa, S. K. Zharmukhamedov, V. V. Klimov and S. I. Allakhverdiev, *Photosynth. Res.* **93**, 133–138 (2007).

* Present Address: Shin-Etsu Chemical Co., Ltd., 28-1 Nishifukushima, Kubiki-ku, Joetsu 942-8601

† Present Address: Institute of Basic Biological Problems, Russian Academy of Sciences, Pushchino, Moscow Region 142290, Russia

Chemistry of Bowl-Shaped Aromatic Compounds and Metal Nanocluster Catalysts

Research Center for Molecular Scale Nanoscience
Division of Molecular Nanoscience

SAKURAI, Hidehiro	Associate Professor
HIGASHIBAYASHI, Shuhei	Assistant Professor
KAMIYA, Ikuyo	IMS Fellow
YARASI, Soujanya	Visiting Scientist
REZA, A. F. G. Masud	Graduate Student
KITAHARA, Hiroaki	Graduate Student
ONOGI, Satoru	Graduate Student
NAKANO, Sachiko	Technical Fellow
KAI, Noriko	Technical Fellow
SASAKI, Tokiyo	Secretary

Bowl-shaped π-conjugated compounds including partial structures of the fullerenes, which are called "buckybowls," are of importance not only as model compounds of fullerenes but also as their own chemical and physical properties. Heteroatom-containing buckybowls (heterobuckybowls) have also been expected to exhibit unique physical characters. For example, in solution they show the characteristic dynamic behavior such as bowl-to-bowl inversion. On the other hand, they sometimes favor stacking structure in a concave-convex fashion in the solid state, giving excellent electron conductivity. Furthermore, some buckybowls are conceivable to possess the bowl-chirality if the racemization process, as equal as bowl-to-bowl inversion, is slow enough to be isolated. However, very few buckybowls/heterobuckybowls has been achieved for preparation mainly due to their strained structure, and no report on the preparation of chiralbowls has appeared. In the present project, we develop the rational route to the various kinds of buckybowls/heterobuckybowls with perfect chirality control using the organic synthesis approach.

We also investigate to develop novel catalytic properties of metal nanoclusters. We focus on the following projects: Preparation of size-selective gold nanoclusters supported by hydrophilic polymers and its application to aerobic oxidation catalysts: Synthetic application using metal nanocluster catalyst: Development of designer metal nanocluster catalyst using the highly- functionalized protective polymers: Catalytic activity of metal nanoclusters under the laser-irradiated conditions.

1. Asymmetric Synthesis of a Chiral Buckybowl, Trimethylsumanene[1)]

Many buckybowls possess "bowl chirality" derived from their three-dimensional geometry, similar to chiral fullerenes and carbon nanotubes. Methods to control the bowl chirality can potentially be applied to the related chiral fullerenes and carbon nanotubes as well. In addition, chiral aromatic compounds are expected to contribute to a variety of applications such as asymmetric molecular recognition, homochiral crystal organic materials, and chiral ligands for organometallic catalysis. Asymmetric synthesis of chiral buckybowls is challenging since synthetic strategies have not yet been established. We developed the first rational asymmetric synthesis of a C_3 symmetric chiral buckybowl, (*C*)-8,13,18-trimethylsumanene (**1**).

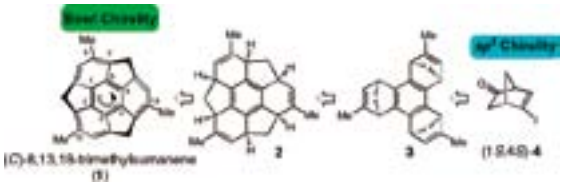

Scheme 1. Strategy for the asymmetric synthesis of (*C*)-**1**.

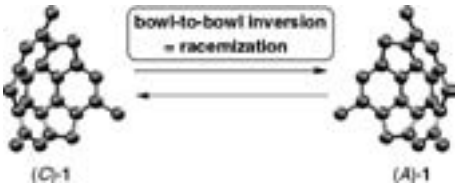

Figure 1. Racemization of **1** through a bowl-to-bowl inversion.

The bowl-to-bowl inversion energy barrier must be taken into account at this step, because this inversion corresponds to a racemization process for a chiral buckybowl (Figure 1). The bowl-to-bowl inversion energy barrier of **1** is estimated to be ca. 21 kcal/mol. Since the energy barrier corresponds to ca. 2 h half-life time of racemization at 0 °C, the aromatization step must be carried out at a low temperature. The bowl-shaped structure of **2** could be constructed from a benzonorbornene derivative **3** utilizing a tandem ring-opening/closing olefin metathesis approach. The benzonorbornene derivative **3** could be obtained by cyclotrimerization of a chiral halonorbornene derivative (1*S*,4*S*)-**4**. By adopting this approach, the bowl

chirality of **1** is controlled by the sp^3 chirality of the starting norbornene derivative. Synthetic route to (*C*)-**1** is listed in Scheme 2.

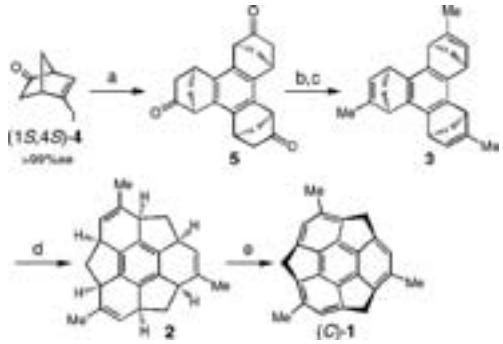

(a) $Pd(OAc)_2$ 5 mol%, PPh_3 10 mol%, Bu_4NOAc 1000 mol%, Na_2CO_3, MS 4 Å, 1,4-dioxane, 100 °C, 2 h, 55%; (b) $NaN(SiMe_3)_2$ 350 mol%, $(2,6\text{-}diMePhO)_2P(O)Cl$ 350 mol%, $P(O)(NMe_2)_3$ 350 mol%, THF, –80 °C, 75%; (c) $Pd(OAc)_2$ 5 mol%, $PCy_3{\cdot}HBF_4$ 10 mol%, MeMgI 400 mol%, THF, 40 °C, 2 h, 72%; (d) Grubbs 1st generation catalyst 50 mol%, CH_2Cl_2, under ethylene, 40 °C, 6 h, then Grubbs 2nd generation catalyst 50 mol%, CH_2Cl_2, 40 °C, 12 h, 24%; (e) DDQ 600 mol%, CH_2Cl_2, 0 °C, 1 min 68%.

Scheme 2. Synthesis of (*C*)-8,13,18-trimethylsumanene (**1**).

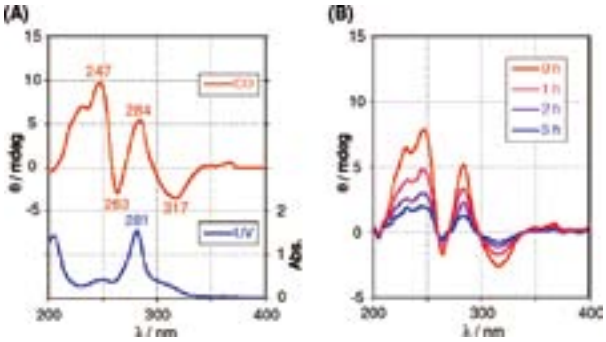

Figure 2. (A) CD spectra of (*C*)-**1** in CH_3CN at –40 °C (red line) and UV spectra of (±)-**1** in CH_3CN at rt (blue line); (B) decay of CD spectra of (*C*)-**1** in CH_3CN at 10 °C for 3 h.

The chirality of thus-obtained (*C*)-**1** was confirmed by measurement of the circular dichroism (CD) spectra. The intensity of the CD spectra at –40 °C scarcely changed but gradually decreased at 10 °C (Figure 2). The bowl-to-bowl inversion energy barrier of **1** in CH_3CN was determined to be 21.6 kcal/mol by tracing the decay of the CD spectra at 247 and 282 nm at 10 °C (Supporting Information). This value is in good accordance with the estimated one.

To determine the enantiomeric excess of synthetic **1**, we needed to derivatize **1** while avoiding racemization through a bowl-to-bowl inversion. Selective introduction of trimethylsilyl groups at the *exo* positions of the dibenzylic positions induces new sp^3 chirality which prevents the enantiomers from racemizing (Scheme 3). However, we were unable to separate the enantiomers of **6** using chiral HPLC. Instead, (*S*)-$Ph(CF_3)$(OMe)CCO groups were introduced to create diastereomers. Finally the enantiomeric excess of **1** was determined as 90% ee based on the ^1H NMR analysis of the diastereomeric ratio of **7**.

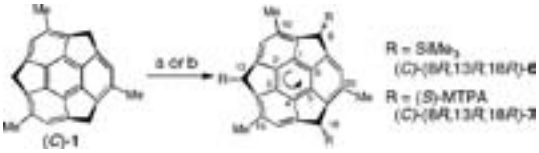

(a) (±)-**1**, LDA 1000 mol%, THF, 0 °C then Me_3SiCl 1000 mol%, (±)-**6** 45%; (b) (*C*)-**1**, LDA 600 mol%, THF, –40 °C, then (*R*)-$Ph(CF_3)(MeO)CCOCl$ = (*R*)-MTPACl 1000 mol% 17%.

Scheme 3. Determination of the enantiomeric excess of **1**.

2. Thermosensitive Gold Nanoclusters Stabilized by Well-Defined Vinyl Ether Star Polymers: Reusable and Durable Catalysts for Aerobic Alcohol Oxidation[2)]

Au nanoclusters of less than 4 nm with a narrow size distribution were prepared and supported in thermosensitive vinyl ether star polymers (Au@star poly(EOEOVE)$_{200}$) obtained by living cationic polymerization. The thermosensitivity of the star polymers permitted easy separation of the clusters from the reaction mixture without any negative aggregation. Thus, the Au clusters could be recovered for reuse several times to induce alcohol oxidation with similar reactivity in each run.

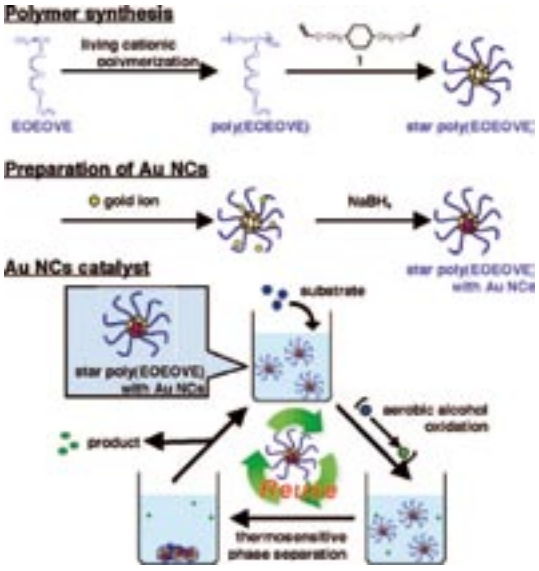

Scheme 4. Preparation and Catalytic Use of Au NCs.

References

1) S. Higashibayashi and H. Sakurai, *J. Am. Chem. Soc.* **130**, 8592–8593 (2008).

2) S. Kanaoka, N. Yagi, Y. Fukuyama, S. Aoshima, H. Tsunoyama, T. Tsukuda, and H. Sakurai, *J. Am. Chem. Soc.* **129**, 12060–12061 (2007).

Multifunction Integrated Macromolecules for Molecular-Scale Electronics

Research Center for Molecular Scale Nanoscience
Division of Molecular Nanoscience

TANAKA, Shoji Assistant Professor

To date there have been demonstrations of molecular-scale diode, switches, transistors, logic circuits, and memory cells, however, the fabrication of complete molecular-scale electronic circuits remains challenging because of the difficulty of connecting molecular device elements to one another. To overcome this problem, we have been developing step-wise synthetic protocols for integrating the molecular functional units required for advanced information processing within a single macromolecule. Our strategy is based on modular architecture using a library of versatile molecular building blocks. The flexible functionality of these blocks is derived from the 3,4-diaminothiophene component, which can be easily modified to tune the structural and electronic properties of the main π-conjugated chain.

1. Thiophene Oligomers for Single-Molecule Charge-transport Measurements

One of the current issues in molecular-scale electronics is to understand and control the charge transport characteristics of single-molecular wires bonded between metal electrodes. To this end, we have synthesized a series of precisely defined oligothiophenes (**1**) ranging in length from 1 to 30 nanometers. These molecular wires have thiocyanate (**-SCN**) anchors that can lead to spontaneous assembly of the wires on Au-based nano-gap electrode systems without activation agents. The systematic nano-scale charge transport measurements using STM break junctions or planar nano-gap electrode systems are now in progress.

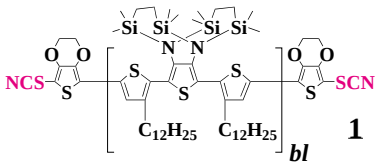

***bl* = 1, 2, 3, 4, 5, 6, 7, 8, 10,16, 24**
(*l* = 1 ~ 30 nm)

Figure 1. Structures of oligomers (**1**).

2. Electrical Conductance of Oligothiophene Molecular Wires[1)]

A break junction method using a scanning tunneling microscope has been applied to electrical conductance measurement of newly designed oligothiophene molecules terminated with a thiocyanate group. The tunneling conduction was evident from an exponential decay of the conductance as a function of the molecular length up to ca. 6 nm. The tunneling decay constant was estimated to be 0.1 angstrom^{-1}. The pre-exponential factor was 1.3 × 10^{-6} S, which was smaller than that observed for alkanedithiols.

3. Direct Conformational Analysis of a 10nm Long Oligothiophene Wire[2)]

Conformational variations of a 10 nm long oligothiophene wire (**2**) on Au(111) have been directly visualized by scanning tunneling microscopy (STM). The local bending angles within the wire are well characterized as s-cis/s-trans configurations of individual thiophene rings. We find that the partial stabilization of the metastable s-cis conformation results in the wire bending, which should be influenced by solvent and substituents.

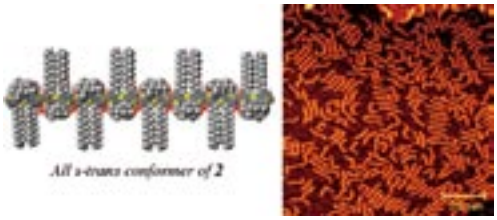

Figure 2. Structure of oligomer (**2**) and Large-area STM image.

References

1) R. Yamada, H. Kumazawa, T. Noutoshi, S. Tanaka and H. Tada, *Nano Lett.* **8**, 1237–1240 (2008).
2) F. Nishiyama, K. Ogawa, S. Tanaka and T. Yokoyama, *J. Phys. Chem. B* **112**, 5272–5275 (2008).

Development of Novel Heterocyclic Compounds and Their Molecular Assemblies for Advanced Materials

Safety Office

TOMURA, Masaaki Assistant Professor

Heterocycles containing sulfur and/or nitrogen atoms are useful as components of functional organic materials since heteroatoms in their rings are helpful to stabilize ions or ion-radical species. In addition, intermolecular interactions caused by heteroatom contacts can be expected to form unique molecular assemblies. In this project, novel functional organic materials based on various heterocycles were synthesized and their physical and structural properties were investigated.

1. Construction of Molecular Networks Using Chloranilic Acid[1)]

In the crystal structure of 4-cyanopyridinium hydrogen chloranilate, the centrosymmetric dimmers with O–H···O hydrogen bonds are linked by intermolecular N–H···O and N···Cl interactions to construct a two-dimensional large square grid molecular network (Figure 1).

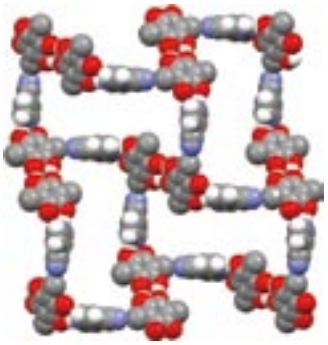

Figure 1. A two-dimensional large square grid molecular network.

2. Photooxidation and Reproduction of Pentacene Derivatives Substituted by Aromatic Groups[2)]

Pentacene derivatives substituted by aromatic groups at the 6,13-positions were prepared and investigated for their electronic properties and the photooxidation–deoxygenation.

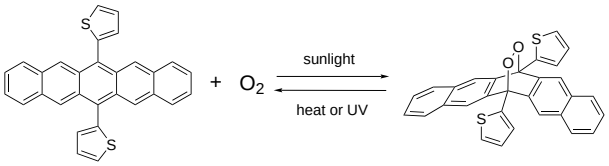

3. X-Ray Crystallographic Analyses of Heterocyclic and Aromatic Compounds[3–9)]

The X-ray crystallographic analyses of seven heterocyclic and aromatic compounds have revealed their interesting structural natures and unique molecular aggregations.

References

1) M. Tomura and Y. Yamashita, *Anal. Sci.* **24**, x31–x32 (2008).
2) K. Ono, H. Totani, T. Hiei, A. Yoshino, K. Saito, K. Eguchi, M. Tomura, J. Nishida and Y. Yamashita, *Tetrahedron* **63**, 9699–9704 (2007).
3) M. Tomura, K. Ono, M. Kaiden, K. Tsukamoto and K. Saito, *Acta Crystallogr., Sect. E* **63**, o4568–o4569 (2007).
4) K. Ono, M. Tomura and K. Saito, *Acta Crystallogr., Sect. E* **63**, o4612–o4612 (2007).
5) M. Tomura, *Acta Crystallogr., Sect. E* **64**, o170–o171 (2008).
6) M. Tomura, H. Yamaguchi, K. Ono, M. Kaiden and K. Saito, *Acta Crystallogr., Sect. E* **64**, o172–o173 (2008).
7) K. Ono, M. Tomura and K. Saito, *Acta Crystallogr., Sect. E* **64**, o468–o468 (2008).
8) M. Tomura and Y. Yamashita, *Acta Crystallogr., Sect. E* **64**, o545–o545 (2008).
9) K. Ono, K. Tsukamoto, M. Tomura and K. Saito, *Acta Crystallogr., Sect. E* **64**, o1069–o1069 (2008).

Visiting Professors

Visiting Professor
BABA, Yoshinobu *(from Nagoya University)*

Biomolecular Imaging by Quantum Dot

We developed the nanofluidic technology for real-time monitoring of interaction between a quantum dot (Qdot)-labeled single DNA molecule and a protein molecule during enzymatic reaction. A Qdot-labeled single DNA molecule is flowing at ca. 20 μm s^{-1} wherein the microchannel without enzyme patterning, but at the enzyme patterning region, we found a DNA molecule is stopped for several seconds to react with enzyme. We measured over 200 DNA molecules and found that a DNA molecule needs 2 second to search a cleavage sequence of DNA and 3 seconds to induced fit and cut a DNA molecule. The kinetic constant evaluated based on the single molecular measurement is consistent with the value evaluated by the conventional measurements.

Visiting Professor
AWAGA, Kunio *(from Nagoya University)*

Research on Organic Radical Materials

Organic radicals are key materials in both solid-state and solution redox processes. Organic radical solids always exhibit semiconductive behavior, due to electrostatic repulsion between unpaired electrons and/or electron-lattice interactions. This strongly suggests a potential application of organic radicals to organic electronics. We are performing fundamental research on electrical and magnetic properties of organic radical solids and application research on photo- and current-induced phenomena. We are also working on solid-state electrochemistry of insoluble self-assembled organic thin-films and transition metal complex clusters, targeting rechargeable batteries, functional electrodes, and electrochromic devices.

Visiting Associate Professor
HIGUCHI, Masayoshi *(from National Institute for Materials Science)*

Organic-Metallic Hybrid Polymers with Multi-Color Electrochromic Functions

Organic-metallic hybrid polymers are expected to have unique electrochemical, photochemical, magnetic, or catalytic properties based on strong interaction between organic modules and metal ions. Novel hybrid polymers are formed by complexation of metal ions such as Fe(II), Co(II), and Ru(II) with bis(terpyridyl)benzenes as an organic module. The polymers have specific colors based on the metal-to-ligand charge transfer and the color disappears by electrochemical oxidation of the polymer. The electrochromic properties are caused by electrochemical redox of metal ions in the polymers. We found that a film of the hybrid polymer including two different kinds of metal ions in the polymer chain shows multi-color electrochromic change at redox potentials of the metal ions. The hybrid polymers with excellent electrochromic functions will be applied to “multi-color electronic papers,” one of next generation displays.